Radiation-induced conductivity of Al_2O_3: Experiment and theory

R. W. Klaffky, B. H. Rose,* A. N. Goland, and G. J. Dienes
Brookhaven National Laboratory, Upton, New York 11973
(Received 1 August 1979)

The steady-state radiation-induced conductivity (RIC) has been measured in single-crystal Al_2O_3 samples maintained at elevated temperatures during continuous irradiation with 1.5-MeV electrons. As the temperature increases from 300 to 1300 K there are regions in which the RIC increases rapidly, with activation energies between 0.6 and 4.3 eV, and regions in which it slowly decreases with an activation energy of approximately 0.1 eV. A theoretical model is presented in which the rapid increases observed in the RIC are correlated with the thermal detrapping of electrons. In undoped Meller and Linde samples the RIC is controlled by trapping and detrapping from high concentrations of shallow (0.57 and 0.72 eV) electron traps. In 0.004- and 0.03-wt.%-Cr_2O_3-doped samples there is a sufficient concentration of 1.2-eV Cr^{3+} electron traps to prevent the RIC from increasing at low temperatures. To account for the decreases in the RIC, additional rate equations describing the thermal quenching of the conductivity by hole release are considered. The RIC data of the undoped samples indicate that hole release from 0.77-eV V_{OH}^{-} centers may be thermally quenching the conductivity. The results of an isochronal annealing study of the Cr^{4+} EPR signal intensity in a 0.004-wt.%-Cr_2O_3-doped sample and an undoped Linde sample are correlated with thermally-stimulated-current (TSC) measurements to show that electron release from the 0.72-eV trap at low temperatures is followed by hole release from the 0.77-eV V_{OH}^{-} centers at higher temperatures, in agreement with the assumptions of the thermal-quenching model. The RIC data of a 0.004-wt.%-Cr_2O_3-doped sample indicate that the bulk electron-hole recombination rate at room temperature is less than 9×10^{-11} cm^3/sec (electron-capture cross section $<7\times10^{-18}$ cm^2) assuming an electron mobility of 1 cm^2/V sec. Since this recombination rate is significantly lower than the Langevin rate of 2×10^{-7} cm^3/sec for diffusion controlled bulk recombination, it is likely that bulk electron-hole recombination occurs predominantly at repulsive hole centers such as V_{OH}^{-} centers. There are several mechanisms other than thermal quenching which could account for the weak decreases in the RIC. These are the LO-phonon scattering of conduction electrons ("large-polaron" mobility) and bulk electron-hole recombination occurring through multiphonon emission.

I. INTRODUCTION

Studies of radiation-induced changes in the properties of Al_2O_3 began twenty years ago.[1-6] Because there are a number of current technological areas where there may be uses for Al_2O_3, its defect properties have again received attention.[7-12] One potential use for Al_2O_3 is as an electrical insulator in fusion devices. In this application the presence of a continuous background radiation level must be considered because dose rates ranging up to 10^4 rad/sec have been estimated to result from the neutron activation of reactor structural materials.[13] The effect of this ionizing radiation is to generate electron-hole pairs within Al_2O_3 leading to a radiation-induced conductivity (RIC).

In order to determine the RIC of Al_2O_3 resulting from dose rates of this magnitude, we have performed steady-state ac electrical-conductivity measurements on single-crystal samples maintained at elevated temperatures during continuous irradiation with 1.5-MeV electrons. There have been steady-state room-temperature RIC measurements of single-crystal Al_2O_3 during γ irradiation[14] and transient RIC measurements during pulsed irradiation.[15,16] This is the first time, however, that the steady-state RIC has been studied over a wide range of temperatures and dose rates.

A theoretical model has been developed which describes the major features of the observed dose rate and temperature dependence of the RIC. It is assumed in the model that the electrons are the dominant charge carriers and that changes in the conductivity result from carrier trapping and thermal detrapping. The increases in the RIC observed with increasing temperature are attributed to the thermal release of electrons from shallow and deep electron traps. Decreases in the conductivity are attributed in the model to the thermal release of trapped holes and a subsequent quenching of the conductivity through recombination of these holes with electrons at the shallow electron traps. Theoretical fits to the RIC data yield activation energies and effective trap concentrations for each sample. Alternative explanations for the decrease in the conductivity including a temperature-dependent mobility resulting from LO-phonon scattering and a temperature-dependent bulk electron-hole recombination rate resulting from multiphonon emission (MPE) are also considered.

A number of secondary measurements are reported. The results of an isochronal annealing

study of the CR^{4+} EPR signal intensity are discussed with reference to the assumption that electron release from shallow traps is followed by hole release at higher temperatures. Finally, thermally-stimulated-current (TSC) activation energies are correlated with the trap activation energies derived from theoretical fits to the RIC data.

II. EXPERIMENTAL METHODS

The RIC measurements were performed on 0.620-in.-diam 0.040-in.-thick Meller Verneuil crystals (Adolph Meller and Co.) and Linde Czochralski crystals (Union Carbide Corporation) undoped and doped with 0.004- and 0.03-wt.% Cr_2O_3. The samples had three rf-sputtered electrodes. A guard electrode was in contact with a grounded platinum cup, as shown in Fig. 1, thus serving to eliminate surface and gas phase conduction between the front and rear electrodes. The rear electrode made contact with a platinum disc held in place by a spring-loaded alumina tube. A Pt–Pt:10-at.%-Rh thermocouple, consisting of 0.001-in.-thick Pt and Pt–10-at.%-Rh foils was sintered onto the front electrode in vacuum. With this thermocouple the temperature of the sample region exposed to electron irradiation could be determined and the thermal equilibrium of the sample assured. Since the thermocouple was in good thermal contact with the sample, a precise determination of the sample temperature could be made while ramping the sample temperature at heating rates up to 0.5 K/sec during TSC measurements. As a result, the temperatures of the TSC maxima were reproducible to better than ±1.0 K.

The entire molybdenum resistance furnace and sample holder assembly was located inside the beam tube of the BNL Dynamitron Accelerator which operated at a pressure of ~10^{-6} Torr. Although the furnace was capable of heating the sample to temperatures of ~1500 K, the maximum operating temperature was limited to 1300 K to prevent excessive platinum evaporation from the electrodes. A uniform collimated 0.95-cm-diam beam was carefully aligned so that it was centered on the sample. A Faraday cup was remotely inserted between the collimator and the sample to measure beam currents ranging from 1 nA to 1 μA. This current range was ideal for the RIC measurements because steady-state conditions were achieved rapidly without serious beam heating effects. The typical precision of the RIC measurements was 10%.

It was necessary to use an ac measurement technique to avoid measuring a dc current contribution from the primary 1.5-MeV electron beam penetrating the sample. A low-frequency (1–15 Hz) signal with constant 15-V peak amplitude was applied to the front electrode as shown in Fig. 2. The resultant ac sample current picked up from the rear electrode was amplified using a Keithley Model 427 current amplifier, then filtered to remove high frequency noise before being detected by an Ortec Model 9501 lock-in amplifier. From a comparison of the sample current to the current resulting from applying the same voltage signal to a General Radio (1×10^6)-Ω standard resistor, the sample resistance was determined. The sensitivity of the measurement was considerably enhanced by applying an 180° out-of-phase voltage to a General Radio Model 1422 variable capacitor to null out the capacitive part of the sample current before amplification.

The TSC measurements were performed using the same sample holder and a.c. measurement technique used in the RIC measurements. The samples were given a dose of approximately 10^7 rad at room temperature and then ramped at rates of 0.1 to 0.5 K/sec. The analog output of the lock-in was recorded by a strip-chart recorder. Signals (1 Hz) of constant 150 V peak amplitude were applied to the samples while they were being thermally ramped. Using this technique, sensitivities of 10^{-12} A were obtained. Since steady-state background peaks can occur in the ac conductivity[17]

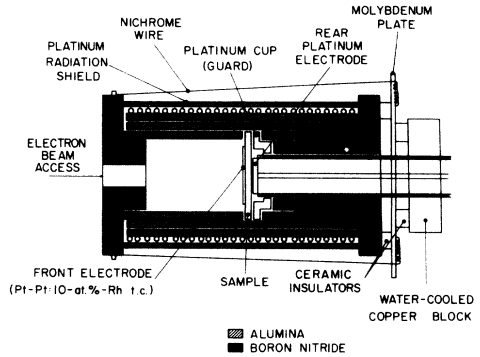

FIG. 1. Sample holder and furnace configuration for performing RIC measurements during electron irradiation at temperatures between 300 and 1200 K.

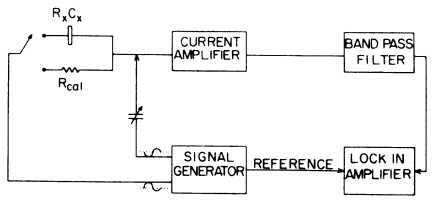

FIG. 2. Block diagram of the low-frequency bridge used to make ac measurements of the electrical conductivity during 1.5-MeV electron irradiation.

that are not related to the TSC peaks, care was taken to ramp the sample twice from 300 to 1300 K following a single exposure to electron irradiation. The first ramp contained the TSC peaks plus the background peak and the second ramp contained only the background peak since the charge traps were emptied by the first ramp. The background peak was then subtracted from the first ramp to determine the correct TSC peaks. At high temperatures, when the background ionic conductivity becomes too large, TSC information could not be obtained. As a result, TSC measurements were limited to temperatures below 1200 K for the Meller sample and 900 K for the doped and undoped Linde samples.

The EPR system used in the studies of Cr^{3+} and Cr^{4+} signal intensities was an X-band homodyne system with a bias arm. Field modulation frequencies were 500 Hz, 4 kHz, or 100 kHz depending on the temperature of the measurements. The magnet system was a 12-in. Varian magnet with a Mark II Fieldial and power supply. The precision of the Cr^{3+} and Cr^{4+} signal intensity measurements was 10%.

Neutron activation analyses were performed on samples and calibration standards exposed to thermal neutrons at the BNL High Flux Beam Reactor for 1 min and for 7.5 h at a thermal neutron flux of $\simeq 1\times10^{14}$ $cm^{-2}sec^{-1}$, respectively. After each exposure, the samples were measured using an Ortec Ge(Li) diode detector of 1.8-keV resolution connected to a Nuclear Data ND 2400 multichannel analyzer. The data were analyzed on a computer to determine the major γ-ray peaks. A comparison of the γ-ray peak intensities in the samples to the intensities present in the standards led to a determination of the sample impurity levels. In cases where the sample did not display a γ-ray peak present in the standards, a meaningful upper limit could usually be set on the impurity level in the samples. The standards used in this study were U.S. Geological Survey standards G-2, GSP-1, AGV-1, PCC-1, DTS-1, and BCR-1.

III. RESULTS

A. Radiation-induced conductivity: Dose-rate dependence

For each sample the dose-rate dependences of the RIC were obtained over a wide range of temperatures between 290 and 1300 K. Experimentally, a radiation-induced sample current is measured at a given temperature as a function of incident beam current, as shown in Fig. 3. To ensure that there were no hysteresis effects resulting from failure to attain equilibrium, data points

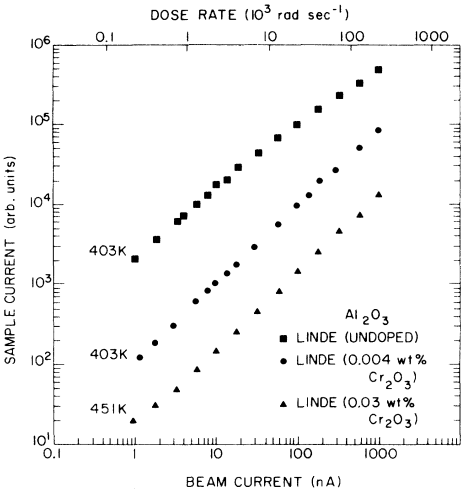

FIG. 3. Plots of the radiation-induced sample current versus primary beam current and dose rate. The dose rate was calculated from the energy-loss tables of Berger and Seltzer (Ref. 18). The beam diameter was 0.95 cm.

were taken while increasing the beam current from 1 nA to 1 μA and while subsequently decreasing the current to 1 nA. No hysteresis effects were observed. In addition to indicating that steady-state conditions applied, the lack of hysteresis indicates that the amount of damage introduced by the 1.5-MeV electron beam over a typical measurement time of 3000 sec is not significant compared to the intrinsic defect and impurity concentrations present in these samples. The dose-rate scale of Fig. 3, proportional to the beam current, was calculated using an energy loss value of 0.63 MeV in Al_2O_3, obtained from energy-loss tables[18] for 0.9- to 1.5-MeV electrons.

It is convenient to relate the radiation-induced conductivity σ to the dose rate R by the approximate phenomenological equation $\sigma=KR^{\delta}$. The exponent δ is directly obtainable from the experimental curve since σ is proportional to the sample current and R to the beam current. For comparison with the theory average δ values $\bar{\delta}_{10}$ and $\bar{\delta}_{100}$ were computed from the experimental σ values at 3, 30, and 300 nA as $\bar{\delta}_{10}=\log_{10}\sigma_{30}-\log_{10}\sigma_{3}$, and $\bar{\delta}_{100}=\log_{10}\sigma_{300}-\log_{10}\sigma_{30}$ where the subscripts refer to incident beam currents in nA. The scatter in the $\bar{\delta}$ values of the undoped and doped samples is typically ±5% resulting from the ±10% scatter in the RIC values. An exception is the ±10% scatter in the Meller $\bar{\delta}_{100}$ values (Fig. 4) which results from the ±20% scatter in the 300-nA RIC values above 600 K (Fig. 7).

The $\bar{\delta}_{10}$ and $\bar{\delta}_{100}$ values for the undoped Meller

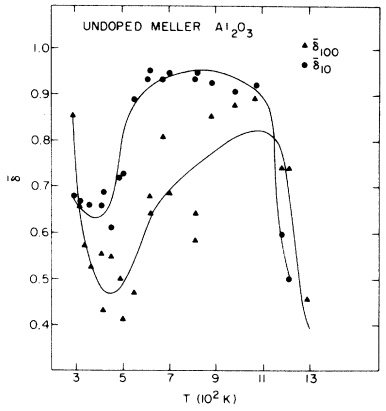

FIG. 4. Temperature dependence of $\bar{\delta}$ values for the Meller Al_2O_3 sample. $\bar{\delta}_{10}$ and $\bar{\delta}_{100}$ represent average values of the slope in log-log plots of the RIC vs dose rate at incident beam currents of 10 and 100 nA, respectively, and are defined as $\bar{\delta}_{10} = \log_{10}\sigma_{30} - \log_{10}\sigma_3$ and $\bar{\delta}_{100} = \log_{10}\sigma_{300} - \log_{10}\sigma_{30}$. The solid lines show the $\bar{\delta}$ values calculated from theoretical fits of the thermal quenching model to the RIC (see Fig. 7).

and Linde samples have a similar temperature dependence as shown in Figs. 4 and 5. Near room temperature both the Meller and the Linde samples exhibit a nonlinear dose-rate dependence with $\bar{\delta}$ values between 0.7 and 0.9. As the temperature increases, the $\bar{\delta}$ values decrease to a minimum. The temperature of the minumum increases with increasing dose rate: the minima in $\bar{\delta}_{10}$ occur at approximately 325 and 400 K in the Linde and Meller samples, respectively, while the minima in $\bar{\delta}_{100}$ occur at 375 and 450 K. At intermediate temperatures the $\bar{\delta}$ values increase to a maximum value of approximately 1.0 corresponding to a linear dose-rate dependence. As the temperature is further increased, the values decrease toward a value of 0.5. The lines shown in these figures correspond to theoretical fits which are based on a trapping model which will be discussed below.

Upon doping the Linde uv grade Al_2O_3 with 0.004-wt.% Cr_2O_3 and 0.03-wt.% Cr_2O_3 the temperature dependence of the $\bar{\delta}$ values is markedly altered as shown in Fig. 6. The $\bar{\delta}$ values of the heavily doped sample are not shown because they are practically the same as those of the lightly doped sample. In this figure only $\bar{\delta}_{10}$ is displayed for the sake of clarity. The $\bar{\delta}_{100}$ values have the same general temperature dependence. For temperatures between room temperature and 700 K, and $\bar{\delta}_{10}$ value is approximately 1.0. As the temperature is increased above 700 K, $\bar{\delta}_{10}$ decreases to a local minimum near 800 K, increases to a maximum near 950 K, and then decreases at the highest temperatures. The RIC of a 0.004-wt.%-Cr_2O_3-doped sample which had been annealed at 1673 K in air for 72 h (oxidized) was also measured. In Fig. 6 the $\bar{\delta}_{10}$ values of this sample are shown for the sake of comparison to the unannealed sample. As a result of annealing, the depression of $\bar{\delta}_{10}$ between 700 and 900 K is substantially reduced. As will be discussed below, these changes result from a redistribution of deep ($\simeq$1-eV) trap concentrations brought about by annealing. In the remainder of this paper, samples which have been annealed in air at 1673 K will be referred to as "oxidized" samples since this treatment is known to produce

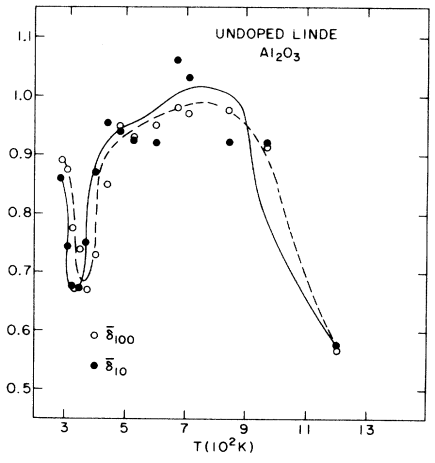

FIG. 5. Temperature dependence of $\bar{\delta}$ values for the undoped Linde Al_2O_3 sample. The solid and dashed lines show the $\bar{\delta}_{10}$ and $\bar{\delta}_{100}$ values calculated from theoretical fits of the thermal quenching model to the RIC (see Fig. 8).

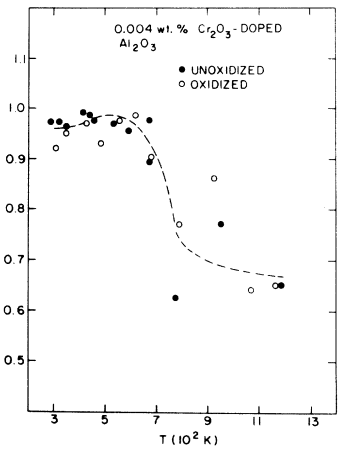

FIG. 6. Temperature dependence of $\bar{\delta}_{10}$ values for the 0.004-wt.%-Cr_2O_3-doped Linde Al_2O_3 sample before and after a 72 h air annealing (oxidation) at 1673 K. The dashed line shows the $\bar{\delta}_{10}$ values calculated from theoretical fits of the thermal quenching model to the RIC data of the unoxidized sample (see Fig. 9).

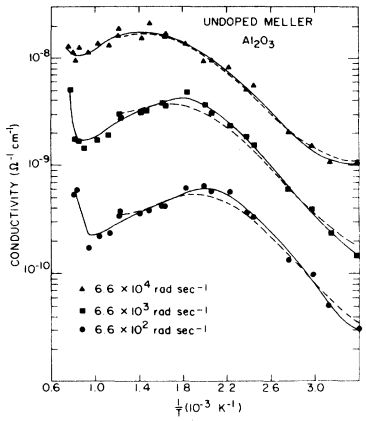

FIG. 7. Temperature dependence of the RIC for the undoped Meller Al_2O_3 sample at the dose rates indicated. The solid lines result from computer fits of the thermal quenching model [Eq. (40)] to the data. The dashed lines result from fitting the simple two-trap model [Eq. (12)] to the data at each dose rate using an empirical expression $\mu = BT\exp(E/kT)$ to describe the large polaron mobility. The average values of B and E were 4.9×10^{-5} cm^2/V sec K and 0.12 eV, respectively.

Al^{3+} vacancies in Al_2O_3 crystals.[10] Most of the RIC measurements were conducted on samples which were annealed in air at 1400 K for 24 h prior to having platinum electrodes sputtered onto them. These samples will be referred to as "unoxidized" samples because substantial Al^{3+} vacancy concentrations are not believed to be introduced by this treatment, although some partial oxidation may have occurred. After each high-temperature anneal, the samples were cooled to room temperature at a rate of ~0.1 K/sec.

B. Radiation-induced conductivity: Temperature dependence

In Figs. 7 and 8 are shown plots of the RIC as a function of $1/T$ for the undoped Meller and Linde samples. Data are shown for the selected dose rates of 6.6×10^2, 6.6×10^3, and 6.6×10^4 rad/sec corresponding to incident beam currents of 3, 30, and 300 nA, respectively. At room temperature the Meller sample has a conductivity of 1.0×10^{-9} Ω^{-1}cm^{-1} at 6.6×10^4 rad/sec which is a factor of 4 less than the value of 4.0×10^{-9} Ω^{-1} cm^{-1} for the Linde sample. This difference will be attributed below to a greater shallow trap concentration in the Meller sample. As the temperature increases, the conductivities of both samples show the same

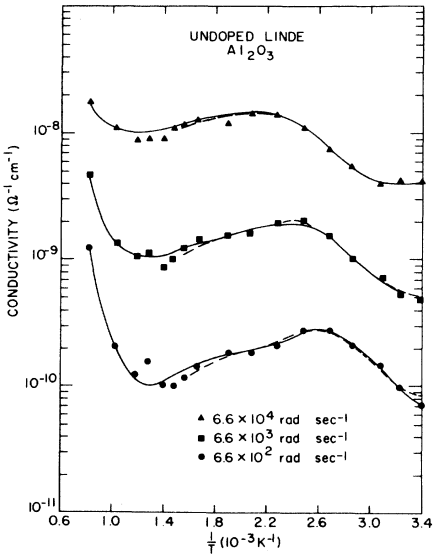

FIG. 8. Temperature dependence of the RIC for the undoped Linde Al_2O_3 sample. The solid lines result from computer fits of the thermal quenching model [Eq. (40)] to the data. The dashed lines result from fitting the simple two-trap model [Eq. (12)] to the data at each dose rate using an empirical expression $\mu = BT\exp(E/kT)$ to describe the large polaron mobility. The average values of B and E were 4.4×10^{-5} cm^2/Vsec K and 0.11 eV, respectively.

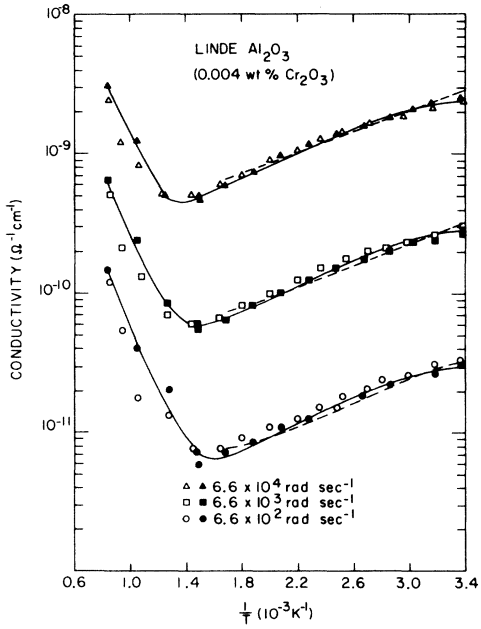

FIG. 9. Temperature dependence of the RIC for the 0.004-wt.%-Cr_2O_3-doped Linde Al_2O_3 sample. The closed symbols correspond to an unoxidized sample. The open symbols correspond to a sample annealed (oxidized) in air for 72 H at 1673 K. The solid lines result from computer fits of the thermal quenching model [Eq. (40)] to the RIC data of the unoxidized sample. The dashed lines result from fitting to the data of the unoxidized sample the empirical expression $\mu = BT\exp(E/kT)$ to describe the large polaron mobility with $B = 5.0\times10^{-5}$ cm^2/V sec K and $E = 0.11$ eV.

general behavior of increasing to a relative maximum, decreasing to a relative minimum and then finally increasing at the highest temperatures. For the Meller sample the relative maximum and minimum, as well as the final increase, occur at higher temperatures than in the Linde sample.

The RIC data for the chromium-doped samples, shown in Figs. 9 and 10, display a distinctly different variation with temperature. As the temperature increases, the RIC of these samples decreases slowly to a minimum followed by a sharp increase at higher temperatures. The temperatures of the minima increase with increasing dose rate. The conductivities of these samples scale approximately inversely with their chromium content. The result of the chromium doping is apparently to introduce a large concentration of deep ($\simeq$1-eV) electron traps since Cr^{3+} ions are believed to predominantly act as electron traps through the reaction $Cr^{3+}+e \rightarrow Cr^{2+}$, although the reaction $Cr^{3+}+h \rightarrow Cr^{4+}$ also occurs. This high concentration of chromium traps overwhelms any effects that these samples' shallow traps might have on the RIC. More specifically, the initial low-temperature increase in the RIC of the undoped samples is not observed in the doped samples.

The changes in the $\bar{\delta}_{10}$ values of a 0.004-wt.%-chromium-doped sample caused by a 72-h 1673-K anneal have been discussed above (see Fig. 6). In Fig. 9 a comparison is made between the temperature dependence of the RIC before and after this annealing. At temperatures below 700 K there is no significant change but at higher temperatures the conductivity is noticeably reduced. As will be discussed below, TSC measurements indicate that the annealing apparently results in an enhanced deep electron trap concentration of unknown species and a reduced concentration of shallower chromium traps. This deep trap redistribution shifts the final increase in the RIC to higher temperatures. This effect will be further investigated during the discussion of the trapping model.

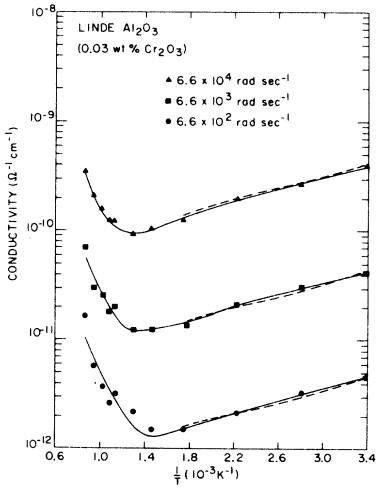

FIG. 10. Temperature dependence of the RIC for the 0.03-wt.%-Cr_2O_3-doped Linde sample. The solid lines result from computer fits of the thermal quenching model [Eq. (40)] to the data. The dashed lines result from fitting to the data the empirical expression $\mu = BT\exp(E/kT)$ to describe the large polaron mobility with $B = 9.5\times10^{-5}$ cm^2/V sec K and $E = 0.09$ eV.

C. Radiation-induced conductivity: Orientation dependence

In order to determine if the RIC had a strong dependence on the orientation of the c axis relative to the applied electric field, a 0.05-wt.%-Cr_2O_3-doped sample, whose c axis was oriented 90 deg from the normal to the sample face, was measured at 300 and 700 K. The RIC of this sample did not deviate more than 5% from the conductivity of a 0.05-wt.%-Cr_2O_3-doped sample with a c axis oriented zero degrees from the normal to the sample face (i.e., a "c-axis" sample). Therefore, at least for these doped samples, the conductivities appear to be insensitive to the c-axis orientation.

D. Thermally-stimulated-current measurements

Thermally-stimulated-current (TSC) measurements were performed on each of the samples described above to determine the relative concentrations of traps present in each sample and the activation energies of these traps.

The TSC peaks of an undoped Meller sample are shown in Fig. 11. The major peaks in the Meller sample occur at approximate temperatures of 396, 509, 728, and 1103 K with minor peaks at 443,

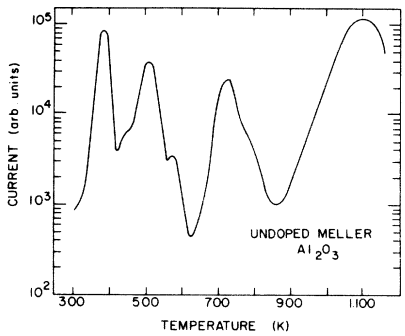

FIG. 11. Thermally-stimulated-current (TSC) peaks observed in the undoped Meller Al_2O_3 sample at a heating rate of 16 K/min. Analysis of the 396- and 1103-K TSC peaks yielded activation energies of 0.72 ± 0.1 and 2.69 ± 0.2 eV, respectively (see Table I).

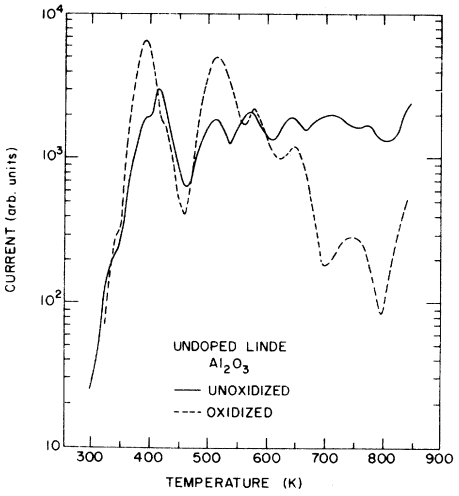

FIG. 12. Thermally-stimulated-current (TSC) peaks observed in the undoped Al_2O_3 sample at a heating rate of 16 K/min before and after a 72-h air annealing (oxidation) at 1673 K. Analysis of the 419-, 509-, and 568-K TSC peaks yielded activation energies of 0.77 ± 0.1, 1.01 ± 0.1, and 1.2 ± 0.1 eV, respectively, for the unoxidized sample (see Table I).

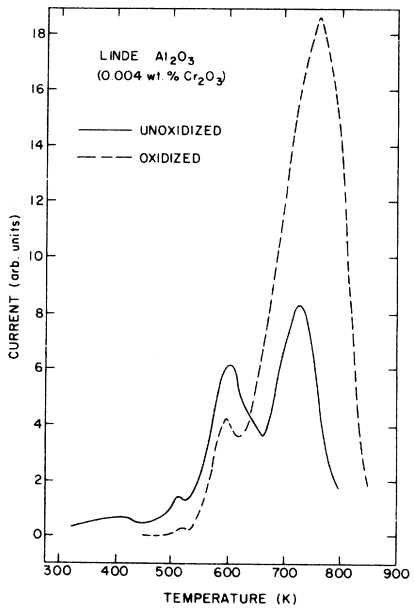

FIG. 13. Thermally-stimulated-current (TSC) peaks observed in a 0.004-wt.%-Cr_2O_3-doped Linde sample at a heating rate of 16 K/min before and after a 72-h air annealing (oxidation) at 1673 K. Analysis of the 728-K TSC peak yielded an activation energy of 1.3 ± 0.1 eV in the unoxidized sample (see Table I).

568, and 773 K. The TSC peaks of undoped Linde samples before and after a 70-h air anneal at 1673 K are shown in Fig. 12. Before the anneal, the Linde sample has a number of peaks of roughly the same magnitude occurring at approximately 396, 419, 509, 568, 728, and 773 K. After the anneal, the 396-K and 509-K TSC peaks were enhanced relative to the other peaks. A slight shoulder near 419 K indicates that this peak is still present although it has been reduced in magnitude.

The TSC results on the Linde samples before and after annealing are similar to the thermoluminescence results of Lee *et al.*[19] on undoped Linde samples. They found that annealing in air at 1623 K for 70 h removed the 419-K peak while producing the 396-, 443-, and 509-K peaks. The 396-, 419-, and 509-K peaks were associated with the decay of V^{2-}, V_{OH}^{-}, and V^{-} hole centers, respectively, by the above authors. Each of these TSC peaks below 600 K will be associated with electron or hole release when the results of an isochronal annealing study of the Cr^{4+} EPR signal strength in a γ-irradiated 0.004-wt.%-Cr_2O_3-doped sample are discussed. We suggest that the similarity of the TSC peaks of the Meller sample to those of the oxidized Linde sample indicates that the Meller sample, the product of a Verneuil process, was probably grown in an oxidizing environment.

The TSC peaks of the 0.004-wt.%-Cr_2O_3-doped sample are shown in Fig. 13 for a sample heated to 1400 K in air before its electrodes were sputtered on, and for a sample heated to 1673 K in air for 70 h. Only a weak 509-K peak is observed in these samples followed by 590- and 728-K peaks at higher temperatures which were also present in the undoped samples. The 590-K TSC peak is associated with the conversion of Cr^{2+} and Cr^{4+} back to Cr^{3+} since at this temperature EPR measurements show that the Cr^{3+} EPR intensity is restored to the value it had prior to room-temperature irradiation and the Cr^{4+} EPR line vanishes. The RIC of these 0.004-wt.%-Cr_2O_3-doped samples can be described theoretically by assuming that the 590- and 728-K TSC peaks are associated with electron release from two deep traps. Unfortunately, there are no experimental studies to the authors' knowledge that have unambiguously associated these TSC peaks with electron or hole release. After the 1673 K anneal, the amount of charge trapped in the 728-K trap is enhanced while that in the 590-K trap is reduced. The TSC peaks of a 0.03-wt.%-Cr_2O_3-doped sample annealed at 1400 K were also measured and are similar to the 0.004-wt.%-Cr_2O_3-doped sample annealed at 1400 K.

E. TSC activation energy analysis

In determining the activation energies of the major TSC peaks, the heating rate technique of Hoogenstraaten[20] was used except for the 1073-K

Meller TSC peak which was analyzed using the initial rise technique of Garlick and Gibson[21] because the background ac conductivity was rising rapidly above 1050 K making an accurate determination of the peak temperature difficult. In a recent review article Kivits[22] has shown that both of these techniques give reliable activation energy values independent of the escape frequency factor and the retrapping ratio. The heating rate technique was favored in this study because it was less sensitive to the error introduced by the background ac conductivity of the sample. Also, overlapping TSC peaks can perturb the initial rise portion of a TSC peak especially in cases where the peaks are as close together as the 396-, 419-, and 443-K peaks. An isolated peak was obtained at 419 K for a Linde sample heated to 1000 K in air before its contacts were sputtered on. For this peak an initial rise value of 0.73 eV was obtained compared to the 0.77 eV heating rate value. Our activation energies of 0.72 and 0.77 eV for the 396- and 419-K TSC peaks are slightly lower than the values of 0.82 and 0.86 eV reported by Kawamura and Royce[23] for an x-irradiated Linde sample. These authors performed an initial rise analysis of the 365- and 405-K TSC peaks corresponding to our 396- and 419-K peaks. Their TSC peaks occur at lower temperatures because a less rapid heating rate of 0.2 K/sec was employed. It will be shown below that the TSC activation energies derived using the heating rate technique closely correlate with activation energies determined from fitting our model to the RIC data.

Table I lists each TSC peak analyzed, the corresponding activation energy and the sample whose TSC peak was used in the analysis. Values are also shown for the activation energies derived using the expression $E = 25\ kT_m$, where T_m is the temperature of the TSC maximum. Kivits[22] has proposed that this expression gives an approximate value of the activation energy with a maximum deviation of ±30%. The T_m values used were arbitrarily chosen to correspond to a heating rate of approximately 0.3 K/sec. The activation energies derived from this expression agree to within 20% with the values deduced from the heating rate and initial rise techniques.

TABLE I. Summary of TSC peak activation energies.

Sample	T_m (K) ($\beta = 16$ K/min)	E (eV)	$25\ kT_m$ (eV)
Meller	396	0.72 ± 0.1	0.84
Linde (undoped)	419	0.77 ± 0.1	0.90
Linde (undoped)	509	1.01 ± 0.1	1.10
Linde (undoped)	568	1.20 ± 0.1	1.22
Linde (0.004-wt.% Cr_2O_3)	728	1.31 ± 0.1	1.57
Meller	1103	2.69 ± 0.2	2.37

F. Isochronal annealing investigation of Cr^{4+} EPR signal intensity

Although the activation energies of the major charge traps occurring in the undoped and chromium-doped samples have been determined, a full interpretation of the RIC data requires a knowledge of the sign of the charge carriers released from these traps. Using EPR and optical absorption, Turner and Crawford[9] and Lee *et al.*,[19] have associated the 419-K thermoluminescence peak in unoxidized Al_2O_3 with the thermal release of holes from V_{OH}^- centers (i.e., centers consisting of a hole trapped on an oxygen ion adjacent to an Al^{3+} vacancy with an OH^--ion near neighbor). In an oxidized γ-irradiated sample, Lee *et al.*[10] showed that V^- centers (pair of holes trapped adjacent to an Al^{3+} vacancy) anneal out at 383 K and that V^{2-} centers (single hole trapped adjacent to Al^{3+} vacancy) anneal out at 523 K. Since the V^{2-} center concentration was found to increase as the V^- center concentration decreased, these authors attributed the decay of the V^- centers to the thermal release of one of the holes, thus converting V^- centers into V^{2-} centers. It is well known[24] that upon irradiation a fraction of the Cr^{3+} ions in these crystals trap holes creating Cr^{4+} ions which give rise to a $\Delta M = \pm 2$ EPR line observable at 4 K. Small concentrations (<0.2 ppm) of Cr^{5+} have been observed in thermal conductivity and thermally detected EPR measurements[25,26] on Al_2O_3 samples doped with approximately 30 ppm of magnesium. In these studies Cr^{4+} and, to a lesser extent, Cr^{5+} ions were believed to compensate for Mg^{2+} ions. In our undoped and Cr-doped samples we rule out the possibility of significant Cr^{5+} concentrations because we do not anticipate Mg concentrations greater than a few ppm. Therefore the following reactions involving Cr^{4+} are expected to occur below the temperature of 600 K where the Cr^{4+} ion itself becomes thermally unstable:

$$Cr^{3+} + h \rightarrow Cr^{4+}, \quad (1)$$

$$Cr^{4+} + e \rightarrow Cr^{3+}. \quad (2)$$

These reactions indicate that changes in the Cr^{4+} concentration are directly related to the sign of the charge carrier released from traps external to the Cr^{4+} ions. An increase in the Cr^{4+} EPR signal intensity corresponds to hole release [Eq. (1)],

a decrease in intensity corresponds to electron release [Eq. (2)].

In order to identify the sign of the charge released from specific traps, an isochronal annealing study of the Cr^{4+} EPR signal intensity in a 0.004-wt.%-Cr_2O_3-doped sample was performed. The sample was γ irradiated at room temperature and then pulse annealed for 10 min periods at the temperatures shown in Fig. 14. After each anneal the Cr^{4+} EPR intensity was measured at 4 K. Then another pulse anneal was performed at a higher temperature. The $\Delta M = \pm 2$ transition requires that there be a component of the microwave magnetic field (H_{rf}) in the direction of the static magnetic field (H_s), and because the intensity of the transition is sensitive to the angle between them, this angle must be reproducible from measurement to measurement to avoid intensity changes not related to Cr^{4+} concentration changes. A $\frac{1}{8}$-in.$\times\frac{1}{8}$-in.$\times\frac{1}{2}$-in. crystal was cut to a length such that when opposite ends of the crystal touched opposite broad walls of a TE_{102} cavity, the c axis (long dimension) was oriented at 45° with H_{rf}. Then the angular dependence of the Cr^{3+} EPR spectrum was used to orient the static field along the c axis. This fixes H_s at 45° with H_{rf} reproducibly.

In comparing the changes in the Cr^{4+} EPR intensity to the TSC peaks shown in Table I, it should be kept in mind that the effect on the Cr^{4+} EPR signal intensity of a particular charge release will be observed at temperatures below the temperatures of the corresponding TSC peaks. Indeed, one would expect that a large fraction of a trap's charge would be released by annealing the sample for 10 min at a temperature where the TSC intensity is one half of its maximum value. For the 396-, 419-, 443-, and 509-K TSC peaks discussed above, the temperatures of the half-maxima are approximately 368, 403, 423, and 483 K, respectively. It is apparent in Fig. 14 that the temperatures of the half maxima correspond to the maxima and minima in the Cr^{4+} EPR intensity. Therefore, a definite correlation can be made between the TSC peaks and the increases and decreases in the Cr^{4+} EPR intensity. Using the arguments outlined above, the 396-K TSC peak is associated with electron release, since the Cr^{4+} EPR intensity has decreased to a minimum at 368 K. Similarly, the 419-K TSC peak is associated with hole release, the 443-K TSC peak with electron release, and the 509-K TSC peak with hole release.

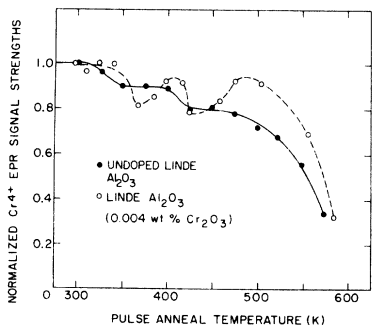

FIG. 14. Isochronal annealing study of the Cr^{4+} EPR intensity. The samples were γ irradiated at room temperature and then pulse annealed for 10 min at the temperatures indicated. After each anneal the Cr^{4+} EPR intensity was measured at 4 K. Open circles and dashed line: data for a 0.004-wt.%-Cr_2O_3-doped Linde Al_2O_3 sample. The minima and maxima in the Cr^{4+} EPR intensity are the result of electron and hole release, respectively, from sites other than Cr^{2+} or Cr^{4+} ions. Solid circles and solid line: data for an undoped Linde Al_2O_3 sample. The lines connect data points.

Our assignment of the 419- and 509-K TSC peaks to hole release is consistent with the assignment of the thermoluminescence peaks observed at these temperatures to hole release from V_{OH}^- centers and V^{2-} centers by Turner and Crawford[9] and Lee *et al.*[10,19] However, Lee *et al.*[10] attributed the decrease in V^- center concentration near 350 K to the thermal release of single holes from V^- centers (two-hole centers) resulting in an increased V^{2-} (one-hole center) concentration. This is clearly inconsistent with a decrease in the Cr^{4+} concentration near 350 K (396-K TSC peak). An alternative explanation would be charge release from an electron trap at this temperature and subsequent recombination with one of the holes at the V^- center. This would also account for the increase in the V^{2-} center concentration seen by Lee *et al.*[10] The nature of the electron traps corresponding to the 396- and 443-K TSC peaks has not been established.

An isochronal annealing study of the Cr^{4+} EPR signal intensity was also conducted on an undoped Linde sample using the experimental procedure described above. The low (~1 ppm) level of chromium present in the undoped sample allows sites other than Cr^{3+} ions to compete effectively for the holes released from V_{OH}^- centers and V^{2-} centers. As a result, increases in the Cr^{4+} concentration cannot be observed (see Fig. 14). However, electron capture by Cr^{4+} ions [Eq. (2)] is expected to be much more likely than hole capture by Cr^{3+} ions [Eq. (1)] because Cr^{4+} ions are attractive trapping centers for electrons while Cr^{3+} ions are neutral trapping centers for holes (Cr^{3+} is the normal lattice charge state). Therefore decreases in the Cr^{4+} EPR intensity resulting from electron capture can be observed in the undoped sample. The temperatures at which the Cr^{4+} EPR intensity decreases in the chromium-doped and undoped samples are closely correlated—the decreases

occur at approximately 350 and 425 K. These results give additional support to the assignment of the 396- and 443-K TSC peaks to electron release.

The final decrease in the Cr^{4+} signal intensity to zero at 573 K corresponds to either hole release from the Cr^{4+} ions or electron capture at the Cr^{4+} ions. The RIC data of the 0.004- and 0.03-wt.%-Cr_2O_3-doped Linde samples can be explained, as will be shown below, by assuming that electrons are the mobile charge carriers and that the 590-K TSC peak corresponds to the thermal release of electrons from Cr^{2+} traps. The recombination of electrons released from Cr^{2+} sites with holes trapped at Cr^{4+} ions would be described by the reaction

$$Cr^{4+} + e \rightarrow (Cr^{3+})^* \rightarrow Cr^{3+} + h\nu, \quad (3)$$

where the excited Cr^{3+} ion releases characteristic R-line emission of energy $h\nu$. This reaction is consistent with the R-line emission that occurs in conjunction with the 590-K TSC peak observed in Cr-doped samples.

Since only the Cr^{3+} and Cr^{4+} ions were observable using EPR we have no direct experimental evidence from which to determine the relative amount of Cr^{2+} ions existing in these samples before the Cr^{2+} and Cr^{4+} charge states anneal out at 600 K. In the case of the 0.004-wt.%-Cr_2O_3-doped sample, no changes were observed in the Cr^{3+} EPR signal intensity between 370 and 470 K, the region where ±15% changes in the Cr^{4+} EPR signal intensity were occurring. This result is expected, however, because γ radiation at room temperature converts only 20% of the Cr^{3+} into Cr^{4+} and Cr^{2+} ions. If one assumes, for example, that all of the Cr^{3+} that is converted is in the Cr^{4+} state, then ±15% changes in the Cr^{4+} EPR intensity would correspond to only ±3% changes in the total Cr^{3+} EPR intensity. These changes, which represent the maximum changes in the Cr^{3+} intensity, are unobservable since the precision of the Cr^{3+} EPR signal intensity is approximately ±10% in the pulsed anneal study where the sample must be repositioned after each annealing step.

G. Neutron-activation analysis

Neutron activation analyses were performed on the undoped Linde and Meller samples and on Linde samples doped with 0.004-wt.% Cr_2O_3 and 0.05-wt.% Cr_2O_3 to determine the major impurities present in these samples. The results are shown in Table II. Upper limits on concentrations were placed where possible. The Linde samples were grown in irridium crucibles which introduces the irridium impurity levels shown in Table II. Other typical impurities which occur in Al_2O_3 starting powders are Ca, Pb, Si, Mg, Ti, and V but these cannot be easily detected in a neutron activation analysis. X-ray fluorescence measurements on these samples showed distinct Ca and Ti peaks. The concentration of these elements could not be determined due to the lack of suitable calibration standards. The large concentration of Fe present in the Meller sample was also detected in the x-ray fluorescence measurements.

TABLE II. Impurity concentrations of Al_2O_3 samples determined from neutron-activation analysis. Units in $\mu g/g$.[a]

Impurity	Linde—undoped	Meller—undoped	Linde—doped with 0.004-wt.% Cr_2O_3	Linde—doped with 0.05-wt.% Cr_2O_3
Ag	0.23	0.26	0.25	0.23
Ce	0.50	0.48	0.13	...
Cr	1.10	1.31	37.5	334.2
Cu	0.25	0.43	0.20	0.35
Eu	0.03	0.01	0.04	0.10
Fe	6.2	38.9	<5.0	<5.0
Ga	3.8	...	0.66	0.62
Gd	<0.04	0.17	<0.04	<0.04
Ir	0.17	...	0.08	0.05
Na	1.5	2.2	3.15	7.37
Nd	<1.0	0.31	<1.0	<1.0
Rb	...	0.67	...	...
Tb	0.05	...	0.04	0.22
Th	<0.3	0.09	0.16	<1.0
Zn	<2.0	<2.0	1.82	<2.0

[a]Concentrations determined using U. S. Geological Survey standards G-2, GSP-1, AGV-1, PCC-1, DTS-1, and BCR-1. Estimated accuracy is about 50%.

IV. THEORY

A. General mechanisms

The electronic conductivity of an insulator is given by

$$\sigma = n_e e \mu_e + n_h h \mu_h, \tag{4}$$

where n_e (n_h) is the concentration of free electrons (holes), e (h) is the charge of the electron (hole), and μ_e (μ_h) is the mobility of the electron (hole). If it is assumed that the electrons are the mobile carriers while the holes are essentially immobile, the conductivity reduces to

$$\sigma = n_e e \mu_e. \tag{5}$$

In the model described in the following sections the mobility is assumed to have a constant value of 1 $cm^2V^{-1}sec^{-1}$ so that variations in the RIC with temperature and impurity and defect concentration result solely from changes in the free-electron concentration. The possible influence of a temperature-dependent mobility will be considered later. For convenience of notation, the free-electron concentration will be specified by e rather than n_e and the concentration of free holes by h.

B. Simple two-trap model

We consider the case where there are two traps (I_1 and I_2) for the electrons and a single hole trap (I_3) for the holes, which also acts as a recombination center. In this simple two-trap model holes are not thermally detrapped from the occupied hole traps (h_3). Then the following kinetic scheme can be used to describe the various processes:

$$\begin{aligned} &\xrightarrow{\phi} e+h, \quad h+I_3 \xrightarrow{K_3} h_3, \\ &e+I_1 \underset{K_{-1}}{\overset{K_1}{\rightleftharpoons}} e_1, \quad e+h_3 \xrightarrow{K_0} I_3, \\ &e+I_2 \underset{K_{-2}}{\overset{K_2}{\rightleftharpoons}} e_2, \quad e+e_1+e_2 = h+h_3, \end{aligned} \tag{6}$$

where ϕ, the effective generation rate of electron-hole pairs, is proportional to the incident flux and is taken to be independent of temperature; K_0 is the electron-hole recombination rate; K_1, K_2, and K_3 are the temperature- and flux-independent trapping rate constants; K_{-1} and K_{-2} are the thermal detrapping rate constants with activation energies E_1 and E_2; e_1, e_2, and h_3 are the concentrations of occupied traps; and I_1, I_2, and I_3 the concentrations of unoccupied traps. The total trap concentrations are $I_1^0 = e_1 + I_1$, $I_2^0 = e_2 + I_2$, and $I_3^0 = h_3 + I_3$. The energy-level diagram for this kinetic scheme is shown in Fig. 15 where the relevant transitions are indicated. The differential equations are

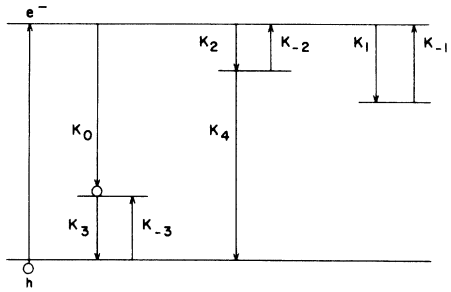

FIG. 15. Energy-level scheme for the two-trap model discussed in the text showing energy-level locations; trapping rates K_1, K_2, and K_3; thermal detrapping rates K_{-1}, K_{-2}, and K_{-3}; electron-hole recombination rate K_0 at the hole traps (I_3^0); and the electron-hole recombination rate K_4 at the electron traps (I_2^0). In the simple two-trap model there is no thermal quenching by hole release ($K_4 = 0$). In the thermal quenching model both K_{-3} and K_4 assume nonzero values.

$$\begin{aligned} &\frac{de}{dt} = \phi - K_1 e I_1 + K_1 e_1 - K_2 e I_2 + K_{-2} e_2 - K_0 e h_3, \\ &\frac{dh}{dt} = \phi - K_3 h I_3, \quad \frac{de_2}{dt} = K_2 e I_2 - K_{-2} e_2, \\ &\frac{de_1}{dt} = K_1 e I_1 - K_{-1} e_1, \quad \frac{dh_3}{dt} = K_3 h I_3 - K_0 e h_3, \end{aligned} \tag{7}$$

where the $K_0 e h_3$ term describes bimolecular recombination at the occupied hole traps h_3. Terms describing direct bimolecular recombination between free electrons and holes are not included since these will only become important at generation rates considerably higher than those attained in this experiment.

It should be noted that these equations are symmetrical in e and h in the sense that if h is the mobile species trapped at I_1 and I_2 the equations are exactly the same if one writes h for e and e for h. Thus, these equations are insufficient for determining from conductivity measurements alone which species carries the current.

In steady state, the rates of change of e, e_1, e_2, and h_3 are zero and

$$\begin{aligned} e_1 &= \frac{I_1^0 e}{(K_{-1}/K_1) + e}, \\ h_3 &= K_3 h I_3^0 / (K_0 e + K_3 h). \\ e_2 &= \frac{I_2^0 e}{(K_{-2}/K_2) + e}, \end{aligned} \tag{8}$$

We assume that both the free-carrier concentration e and the trapped-hole concentration h_3 are much greater than the free-hole concentration h (i.e., $e \gg h, h_3 \gg h$). From the above expression for h_3 it is seen that a significant trapped-hole concentration h_3 will exist if $K_0 e$ is much less

TABLE III. Parameters for calculations with Eq. (12). Trap concentrations in atomic fractions.

ϕ	I_1^0	I_2^0 ($\times 10^{-3}$)	$I_1'^0$	K_0 ($\times 10^7$)	E_1 (K) ($\times 10^3$)	E_2 (K) ($\times 10^3$)	E_1' (K)
10^{-5}	1×10^{-5}	1	...	1	21	6	...
10^{-6}	1×10^{-5}	1	...	1	21	6	...
10^{-7}	1×10^{-5}	1	...	1	21	6	...
10^{-5}	1×10^{-2}	1	...	1	21	6	...
10^{-6}	1×10^{-2}	1	...	1	21	6	...
10^{-5}	1×10^{-3}	1	9×10^{-3}	1	21	6	16×10^3
10^{-6}	1×10^{-3}	1	9×10^{-3}	1	21	6	16×10^3

than or of the same order of magnitude as K_3h. Since we have assumed that $e \gg h$, this implies that $K_3 \gg K_0$. Specific hole traps in Al_2O_3 which could satisfy this condition are Al^{3+} vacancies which have been shown to trap holes on adjacent oxygen ions resulting in V^{2-} centers (single trapped hole), V^- centers (two trapped holes) and $V_{OH}^{\bar{O}H}$ centers (single trapped hole and an adjacent $OH^{\bar{O}H}$ ion). The effective charge of the Al^{3+} vacancy with the above configurations of trapped holes is indicated by each center's superscript. Because these charges are negative with regard to the rest of the crystal, the recombination rate K_0 for electrons with these trapped holes should be very small, as required.

Now, since $h_3 \gg h$, one can ignore h in the charge neutrality condition and

$$\phi = K_3 h I_3 = K_0 e h_3 = K_0 e (e + e_1 + e_2). \tag{9}$$

Therefore,

$$\phi = K_0 e \left(e + \frac{I_1^0 e}{(K_{-1}/K_1)+e} + \frac{I_2^0 e}{(K_{-2}/K_2)+e} \right) \tag{10}$$

or

$$e^2 \left(1 + \frac{I_1^0}{(K_{-1}/K_1)+e} + \frac{I_2^0}{(K_{-2}/K_2)+e} \right) = \frac{\phi}{K_0}, \tag{11}$$

where K_{-1} and K_{-2} are exponential functions of $1/T$. Such a two-trap model will give a double plateau of $\ln e$ vs $1/T$ as detrapping occurs from sites with two different binding energies.

A minimum of e cannot be reproduced by this scheme. However, it turns out that several other important features of the response of the system are little influenced by the existence of the minimum in e. Therefore, it seemed worthwhile to investigate this system, particularly since, to our knowledge, there is no detailed discussion of such a system in the literature.

One can simplify Eq. (11) by ignoring the purely quadratic response except at very high temperature where 1 in the large parentheses is of the same order of magnitude as the other quantities. In the subsequent discussion we shall then use the following as the master equation:

$$e^2 [I_1^0/(e+a) + I_2^0/(e+b)] = \frac{\phi}{K_0}, \tag{12}$$

where

$$a = K_{-1}/K_1 = a_0 \exp(-E_1/T)$$

and

$$b = K_{-2}/K_2 = b_0 \exp(-E_2/T), \tag{13}$$

with $E_1 > E_2$, so that I_1 is the deeper trap.

As illustrative examples numerical calculations were carried out for the parameters listed in Table III ($a_0 = b_0 = 1$ for convenience). The results for $\ln e$ vs $1/T$ are shown in Fig. 16. It is also of interest to calculate δ, defined

$$\delta = \frac{d \ln e}{d \ln \phi} \tag{14}$$

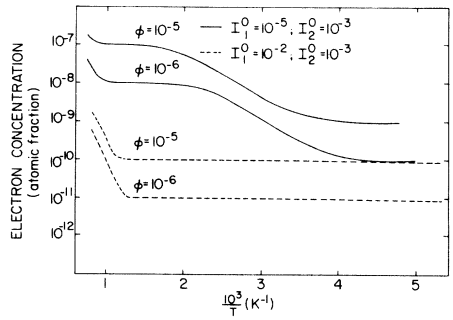

FIG. 16. Temperature dependence of the free-electron concentration calculated using the simple two-trap model [Eq. (12)] with the parameters listed in Table III. The solid lines correspond to a large shallow trap concentration (I_2^0) and the dashed lines to a large deep trap concentration (I_1^0).

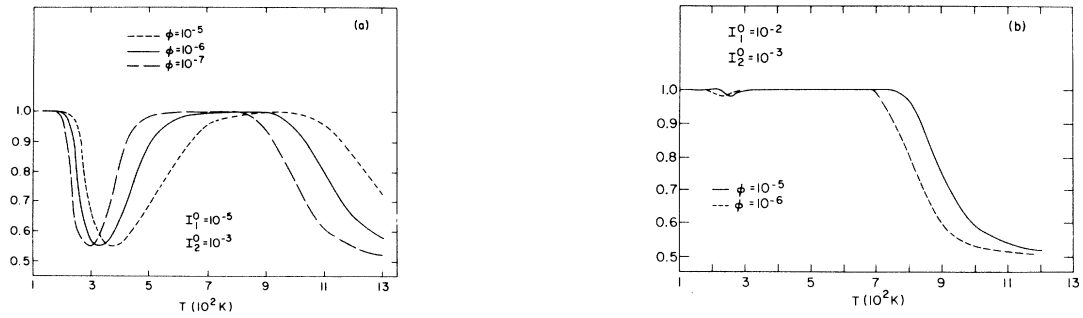

FIG. 17. Temperature dependence of the exponent $\delta = d\ln e/d\ln\phi$ calculated using the simple two-trap model [Eq. (12)] with the parameters shown in Table III. (a) Exponents for the case of a large shallow trap concentration. (b) Exponents for a large deep trap concentration.

as a function of temperature. The δ-vs-T results are shown in Fig. 17. In this instance and in the subsequent discussion, the magnitudes of K_0, ϕ, I_1^0, and I_2^0 are not physically meaningful—they are simply chosen to conveniently illustrate the general features of the temperature and dose rate dependence of e and δ. Later, in discussing the results of computer fits to the conductivity data, proper units will be utilized.

The following features should be noted:

(i) The low-temperature plateau, where $a \ll e$, $b \ll e$, is given by

$$e = \phi/K_0(I_1^0+I_2^0). \tag{15}$$

In this region $\delta = 1$.

(ii) At the high-temperature plateau, where $a \ll e$ but $b \gg e$, and therefore I_2^0/e becomes negligible, we have

$$e = \phi/K_0 I_1^0, \tag{16}$$

and again $\delta = 1$.

(iii) For $I_1^0 > I_2^0$ the difference in the low- and high-temperature plateaus becomes small as the system is overwhelmed by the high concentration of deep traps.

(iv) The "take-off" temperature for increasing e from either plateau decreases with decreasing generation rate ϕ.

(v) Between the two plateaus, δ is between 1 and 0.5; at high temperature, δ approaches 0.5.

Some of these points can be discussed analytically for this simple two-trap model with well separated trapping energies.

The "take-off" temperatures can be estimated as follows. At high temperatures, where $b \gg e$ and I_2^0/b becomes negligible, Eq. (12) becomes

$$e^2 = (\phi/K_0 I_1^0)(e+a), \tag{17}$$

and at the plateau, where $a \cong 0$,

$$e_0 = \phi/K_0 I_1^0, \tag{18}$$

where e_0 is the value of e at the plateau. For a fixed e/e_0 ratio, say A, one obtains, after some algebra,

$$1/T_H = (1/E_1)\ln[K_0 I_1^0/\phi A(A-1)], \tag{19}$$

where T_H is the temperature corresponding to the ratio A. By a similar argument one finds, for the low-temperature "take-off,"

$$1/T_L = (1/E_2)\ln[K_0(I_1^0+I_2^0)/\phi A(A-1)]. \tag{20}$$

These relations show clearly the trends in the "take-off" temperatures with generation rate and trap concentration in full agreement with the graphs in Fig. 16.

The δ-vs-T behavior can be analyzed as follows. From Eq. (12) one obtains, by differentiation,

$$\delta = \frac{d\ln e}{d\ln\phi} = \frac{1}{2-X}, \tag{21}$$

with

$$X = \frac{I_1^0 e/(e+a)^2 + I_2^0 e/(e+b)^2}{I_1^0/(e+a) + I_2^0/(e+b)}. \tag{22}$$

At low temperature, $a \cong 0$, $b \cong 0$, $X \cong 1$, and $\delta = 1$. At temperatures where b is large but a is still near zero $X \to 1$ and $\delta \to 1$. Between these two regimes $x < 1$ and $\delta < 1$, i.e., δ goes through a minimum. At high temperature where $a \gg e$, $x \to 0$, and $\delta \to \frac{1}{2}$. These trends are in full agreement with the detailed calculations illustrated in Fig. 17. The minimum in δ is particularly interesting and can be determined analytically for well separated trapping energies since in this case $a \ll e$ in the region of the minimum. In this region then,

$$X = \frac{1/e+\beta e/(e+b)^2}{1/e+\beta/(e+b)}, \quad \beta = \frac{I_2^0}{I_1^0}. \tag{23}$$

From Eq. (12),

$$e+b = -\beta e^2/(e-C), \quad C = \phi/K_0 I_1^0. \tag{24}$$

Upon substitution in Eq. (23) and rearrangement

$$X=[\beta e^2+(e-C)^2]/\beta eC, \tag{25}$$

and by differentiation with respect to T the condition for X_{min} is given by

$$e^*=C/(1+\beta)^{1/2}, \tag{26}$$

and from Eq. (25),

$$X_{min}=2[(1+\beta)^{1/2}-1]/\beta \tag{27}$$

and

$$\delta_{min}=\beta/2[(1+\beta)-(1+\beta)^{1/2}]. \tag{28}$$

From Eq. (24) one can get b^* and hence T^* as

$$b^*=C=\phi/K_0I_1^0, \quad T^*=\frac{E_2}{\ln(K_0I_1^0/\phi)}. \tag{29}$$

It is important to note from Eq. (28) that δ_{min} depends only on $\beta=I_2^0/I_1^0$ and becomes very small for small β (see Fig. 17) and may become unobservable at high deep-trap concentration. T^*, the temperature at δ_{min}, is a function only of I_1^0/ϕ according to Eq. (29) and increases with increasing ϕ but decreases with increasing I_1^0 (see Fig. 17).

It is also of interest to examine briefly what happens if a third trapping center is present with a binding energy somewhat lower than the I_1^0 high-temperature trap. This additional trap is identified as $I_1^{0'}$ in Table III with binding energy $E_{1'}$. Numerical calculations were done at two flux levels and the results are shown in Figs. 18 and 19. The $\bar{\delta}$ values in Fig. 19 are averages calculated directly from the e values at $\phi=10^{-5}$ and $\phi=10^{-6}$. Since E_1 and $E_{1'}$ are fairly close, a "wiggle" is introduced into the e-vs-$1/T$ curve rather than an additional plateau with e, of course, increased by the additional detrapping. The corresponding change in $\bar{\delta}$ is more striking since an additional minimum is produced by this mechanism at an elevated temperature.

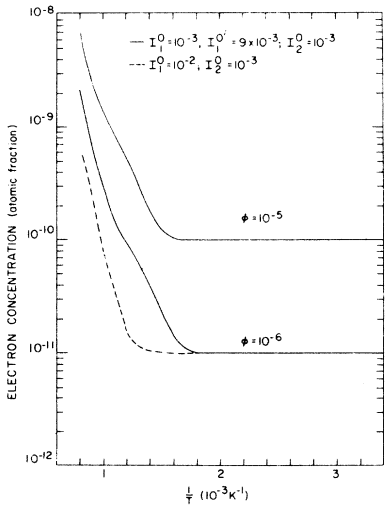

FIG. 18. Temperature dependence of the free-electron concentration calculated from the simple two-trap model. The solid lines represent the case where a second deep trap $I_1^{0'}$ is introduced with a binding energy E_1' slightly lower than the energy E_1 of the I_1^0 traps. The parameters are listed in Table III. The dashed line represents the single deep trap case already displayed in Fig. 16.

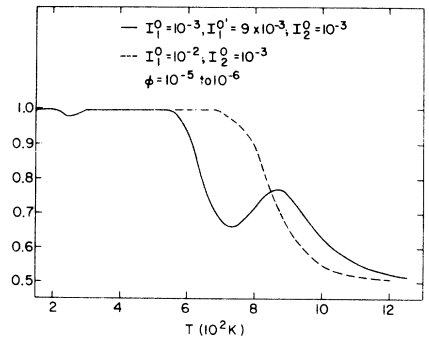

FIG. 19. Temperature dependence of the $\bar{\delta}$ values with a second deep trap (solid line) and without a second deep trap (dashed line). The $\bar{\delta}$ values were computed from the e values displayed in Figs. 16 and 18 at the dose rates $\phi=10^{-5}$ and 10^{-6} (arbitrary units).

C. Temperature-dependent two-trap model (thermal quenching)

As already pointed out, the simple two-trap model cannot simulate a minimum in e as a function of temperature. Empirically it is quite easy to introduce the right sort of temperature dependence by allowing K_0 in Eq. (12) to depend on the temperature. It was assumed, therefore, that K_0 is replaced by

$$K_{00}=K_{01}+K_0^1\exp(-E/T), \tag{30}$$

and numerical calculations were carried out to see if such a scheme simulates the experimental data. K_{01} was taken to be equal to the original K_0 (1×10^7), K_0^1 was assumed to be 273×10^7 and E was chosen to be 4000 K. E_1 and E_2 were the same as in the previous calculation. E should clearly be less than E_2 for simulating a rather shallow minimum in $\ln e$. The temperature dependence of K_0 introduced very little perturbation in the δ-vs-T curves calculated from the simple two-trap model (see Fig. 17). In the e-vs-$1/T$ curves the plateaus of the simple model (Fig. 16) become the maxima of the temperature-dependent model and the minima correspond approximately to the temperature "take-off" points. The low-temperature asymptotes are identical in the two models. It is also important to note that a high value of I_1^0 pushes the maximum to low temperature and renders it shallow. The results are qualitatively very similar to

the experimental data, shown in Figs. 7 through 10. Note in particular that (i) the maxima and minima move to lower temperatures as the dose rate is lowered, and (ii) the maximum, for all practical purposes, can be overwhelmed by increasing the deep trap (I_1^0) concentration.

The actual fit of such a scheme to the experimental data will be discussed in the next section. In the remainder of this section a modified kinetic scheme is outlined in an attempt to relate the above empirical approach to a simple kinetic scheme.

Let the shallow electron trap e_2 also be a recombination center, allow h to be released from the hole trap h_3 (a V_{OH}^- center, for example) as the temperature is raised and let it recombine with e_2. Significant thermal releases of holes will be assumed to occur at a temperature higher than that for release of electrons from e_2 and lower than that for release of electrons from e_1. The following scheme describes the various processes:

$$\xrightarrow{\phi} e+h,$$

$$e+I_1 \underset{K_{-1}}{\overset{K_1}{\rightleftharpoons}} e_1, \quad h+I_3 \underset{K_{-3}}{\overset{K_3}{\rightleftharpoons}} h_3, \quad e+h_3 \xrightarrow[K_0]{} I_3, \tag{31}$$

$$e+I_2 \underset{K_{-2}}{\overset{K_2}{\rightleftharpoons}} e_2, \quad h+e_2 \xrightarrow{K_4} I_2.$$

The corresponding energy-level scheme is shown in Fig. 15. The equations are

$$\begin{aligned}
\frac{de}{dt} &= \phi - K_0 e h_3 - K_1 e I_1 - K_2 e I_2 + K_1 e_1 + K_{-2} e_2, \\
\frac{dh}{dt} &= \phi - K_3 h I_3 + K_{-3} h_3 - K_4 h e_2, \\
\frac{de_2}{dt} &= K_2 e I_2 - K_{-2} e_2 - K_4 h e_2, \\
\frac{de_1}{dt} &= K_1 e I_1 - K_{-1} e_1, \\
\frac{dh_3}{dt} &= K_3 h I_3 - K_{-3} h_3 - K_0 e h_3.
\end{aligned} \tag{32}$$

Recombination now can take place at both h_3 and e_2.

In steady state the rates of change of e, e_1, e_2, h, and h_3 are zero and

$$\begin{aligned}
e_1 &= \frac{eI_1^0}{(K_{-1}/K_1)+e}, \\
e_2 &= \frac{eI_2^0}{(K_{-2}/K_2)+e+(K_4 h/K_2)}, \\
h_3 &= \frac{hI_3^0}{(K_{-3}/K_3)+h+(K_0 e/K_3)}.
\end{aligned} \tag{33}$$

The capture rates K_1, K_2, K_3, K_4 are assumed to be of comparable magnitude while the magnitude of the capture rate K_0 is assumed to be much smaller. Therefore, in the expression for e_2, the term $K_4 h$ can be neglected because $e \gg h$. One can proceed analytically if $K_3 h$ in the expression for h_3 can be neglected with respect to K_{-3} and $K_0 e$. At low temperatures where K_{-3} is negligible this will introduce some error since $K_3 h$ and $K_0 e$ can be of the same order of magnitude. As the temperature increases and K_{-3} becomes large compared to $K_3 h$ and $K_0 e$ the error will be small. With these approximations, one obtains from charge neutrality, neglecting h with respect to h_3,

$$h_3 = \frac{K_3 h I_3^0}{K_{-3}+K_0 e} = e\left(1+\frac{I_1^0}{(K_{-1}/K_1)+e}+\frac{I_2^0}{(K_{-2}/K_2)+e}\right), \tag{34}$$

or

$$h = e\left(1+\frac{I_1^0}{(K_{-1}/K_1)+e}+\frac{I_2^0}{(K_{-2}/K)+e}\right) \times\left(\frac{K_3 I_3^0}{K_{-3}+K_0 e}\right)^{-1}. \tag{35}$$

From setting $dh/dt=0$, one obtains

$$h = \frac{\phi}{K_3 I_3 + K_4 e_2 - (K_3 I_3^0 K_{-3})/(K_0 e + K_{-3})}. \tag{36}$$

Equating this expression to the above expression for h derived from charge neutrality gives

$$e^2\left(1+\frac{I_1^0}{(K_{-1}/K_1)+e}+\frac{I_2^0}{(K_{-2}/K_2)+e}\right) \times\left[K_0+\left(\frac{K_{-3}+K_0 e}{K_{-2}+K_2 e}\right)\frac{K_2 K_4 I_2^0}{K_3 I_3^0}\right]=\phi. \tag{37}$$

At low temperature, where $K_{-2} \ll K_2 e$, $K_{-3} \ll K_0 e$, the term in square brackets in Eq. (37) gives a constant

$$K_{01} = K_0(1+K_4 I_2^0/K_3 I_3^0) = K_0(1+C), \tag{38}$$

where

$$C = K_4 I_2^0 / K_3 I_3^0.$$

At higher temperatures, where $K_{-2} \gg K_2 e$, $K_{-3} \gg K_0 e$, the second term in the second bracket becomes a purely temperature-dependent term. Thus one can identify the empirical expression for the temperature dependence of K_0^1 with that derived by the above kinetic scheme as

$$K_0^1 \exp(-E/T) = C K_2 (K_{-3}/K_{-2})_0 \exp[-(E_3 - E_2)/T]. \tag{39}$$

The above kinetic scheme, of course, need not be unique—there may be many schemes that lead to the same sort of temperature and flux dependence. All we have done really is to relate the purely empirical approach to a simple kinetic scheme. It should also be mentioned that both the

simple and the modified two-trap models are symmetric in e and h and the results are invariant to an exchange of h for e, h_1 for e_1, etc. Thus, there is no way to decide from the model itself as to which carrier is the mobile one. However, the isochronal annealing study of the Cr^{4+} EPR signal intensity discussed above supports the sequence of charge release assumed in the model, i.e., electron release followed by hole release as the temperature increases. It will also be shown below that theoretical fits to the RIC data yield activation energies E_3 for the hole trap that are consistent with the TSC activation energy measured for hole release from V_{OH}^- centers. Therefore, the thermal quenching of the RIC by hole release and subsequent recombination with electrons in shallow traps could be responsible for the observed decreases in the conductivity. Other mechanisms which could cause these decreases will be discussed later.

D. Computer fits of the thermal-quenching model to the RIC data

Detailed RIC data have been presented above for several samples as a function of dose rate ϕ and temperature. These data were fit using a Marquardt nonlinear least-squares fitting procedure described by Bevington[27] to determine if the two-trap model with thermal quenching could reproduce the main features of the data. The final equation used to fit the data was the combination of Eqs. (12) and (30), namely,

$$e^2\left(\frac{I_1^0}{(K_{-1}/K)+e}+\frac{I_2^0}{(K_{-2}/K)+e}\right)=\frac{\phi}{K_{01}+K_0^1\exp(-E/T)}. \tag{40}$$

Since the two-trap model does not account for all of the electron- and hole-trap concentrations present in a sample, the charge neutrality condition [Eq. (6)] is a very crude approximation. As a result, the I^0 values determined from the computer fits only give a rough estimate of the trap concentrations. Also, for the sake of keeping the model simple, the deep trap of concentration I_1^0 was assumed not to be a recombination center so that it is filled at low temperatures [i.e., $e_1=I_1^0$ in Eq. (8)] where there is no thermal detrapping ($K_{-1}/K_1 \ll e$). The deep trap can act as a recombination center, however, resulting in only a fractional occupation at low temperatures. Therefore the I_1^0 values determined from the computer fits should be considered to be effective trap concentrations since they are related to the total trap concentration $I_{1'}$ by $I_1^0=\alpha I_{1'}(0<\alpha<1)$.

A consideration of the Cr^{3+} impurity concentration present in the doped and undoped samples illustrates this point. EPR measurements of the Cr^{3+} signal intensity in the undoped, the 0.004-wt.%-Cr_2O_3-doped and the 0.03-wt.%-Cr_2O_3-doped Linde samples before and after γ irradiation at room temperature indicate that there is 46(±5)%, 24(±5)%, and 17(±5)% reduction of the Cr^{3+} signal intensity after γ irradiation, respectively. If most of the Cr^{3+} is converted to Cr^{2+} through electron capture, then the respective α values of these samples for this deep (1.2-eV) electron trap would be 0.46, 0.24, and 0.17. The I_1^0 effective trap concentrations of 2.6×10^{17} and 1.8×10^{18} cm^{-3} shown in Table IV for the 0.004-wt.%-Cr_2O_3-doped samples were obtained by multiplying the total concentration of chromium atoms present in these samples times an average α value of 0.20.

By holding the above I_1^0 values of the chromium-doped samples constant while performing computer fits to the data, electron-hole recombination rates K_{01} were determined. The RIC of the undoped Linde and Meller samples were then fit after assuming they had the same value of K_{01} as the 0.004-wt.%-Cr_2O_3-doped sample had at the 300 nA beam current (9.5×10^{-11} cm^3sec^{-1}). This assumption, which also introduces additional uncertainty in the I_1^0 and I_2^0 values, was necessary because the effective shallow and deep trap concentrations are not known for the undoped samples. The electron-hole generation rates ϕ corresponding to the 6.6×10^2, 6.6×10^3, and 6.6×10^4 rad sec^{-1} dose rates were calculated to be 4×10^{15}, 4×10^{16}, and 4×10^{17} electron-hole pairs sec^{-1} assuming that each pair requires an energy of approximately twice the band-gap energy (9 eV) to be created which is the primary yield value measured for another wide band-gap material SiO_2 (8.5-eV band gap).[28] At low applied electric fields the creation of each electron-hole pair can require several times this energy. Since accurate yield values have not been measured for high energy (1.5 MeV) electron excitation in Al_2O_3, a value of twice the band-gap energy was used. The parameters shown in Table IV are the result of averaging the parameters obtained from computer fits to the RIC at each of these generation rates. The fitting procedure followed in arriving at these values will now be described.

1. Chromium-doped samples

In fitting the RIC of the doped samples it was assumed that $I_1^0 \gg I_2^0$ so the term $I_2^0/(K_{-2}/K_2+e)$ in Eq. (40) could be neglected. Then I_1^0, K_{01}, K_0^1, K_{-1}/K_1, E_1, and e were determined by fitting the data over the entire temperature range. The resulting parameters are shown in Table IV. The goodness of

TABLE IV. Parameters of the two-trap model with thermal quenching.

Sample	I_1^0 (cm^{-3})	I_2^0 (cm^{-3})	K_{01} [a] (cm^3sec^{-1})	K_0^1 (cm^3sec^{-1})	$\log_{10}(K_{-1}/K_1)_0$ [b]	$\log_{10}(K_{-2}/K_2)_0$ [b]	E_1 (eV)	E_2 (eV)	E (eV)
Linde (undoped)	$(3.4 \pm 1.0) \times 10^{15}$	$(2.9 \pm 1.9) \times 10^{16}$	9.5×10^{-11}	$(5.1 \pm 0.2) \times 10^{-9}$	17.5 ± 1.3	20.7 ± 0.3	1.5 ± 0.3	0.70 ± 0.02	0.05 ± 0.02
Meller (undoped)	$(3.0 \pm 0.6) \times 10^{15}$	$(4.4 \pm 2.6) \times 10^{17}$	9.5×10^{-11}	$(5.1 \pm 0.2) \times 10^{-9}$	27.4 ± 1.7	18.4 ± 0.5	4.3 ± 0.5	0.57 ± 0.06	0.10 ± 0.02
Linde (0.004-wt.% Cr_2O_3)	2.6×10^{17}	...	$(8.6 \pm 0.8) \times 10^{-11}$	$(5.9 \pm 0.5) \times 10^{-9}$	16.9 ± 0.9	...	1.0 ± 0.1	...	0.13 ± 0.01
Linde (0.03-wt.% Cr_2O_3)	1.8×10^{18}	...	$(5.7 \pm 0.2) \times 10^{-11}$	$(1.5 \pm 0.5) \times 10^{-9}$	14.1 ± 0.7	...	1.1 ± 0.1	...	0.08 ± 0.01

[a] K_{01} was determined after assuming an electron mobility $\mu_e = 1\ cm^2V^{-1}sec^{-1}$.
[b] $(K_{-1}/K_1)_0$ and $(K_{-2}/K_2)_0$ are in cm^{-3}.

fit is illustrated in Fig. 9 and Fig. 10 in plots of $\log_{10}\sigma$ vs $1000/T$ and in Fig. 6 for $\bar{\delta}$ vs T. The extra shoulder in the data between 600 and 1000 K at the lowest ϕ (particularly for the lightly doped sample) suggests the presence of two high-temperature traps (in this connection see Fig. 18 of the simple two-trap model without thermal quenching). There is a corresponding wiggle in the high-temperature $\bar{\delta}$ vs T data (Fig. 6) as predicted by the simple model (see Fig. 19). No attempt was made to improve the fit by introducing a third electron trap. TSC measurements on the lightly doped sample also provided evidence of two deep traps that thermally empty in this temperature range (see Fig. 13). The traps had activation energies of 1.2 ± 0.1 and 1.3 ± 0.1 eV. By oxidizing the sample at 1673 K for 70 h it was possible to enhance the occupation of the 1.3-eV trap at the expense of the 1.2-eV trap. The effect of oxidation of the σ-vs-$1000/T$ and $\bar{\delta}$-vs-T curves of the lightly doped sample, shown in Figs. 9 and 6, closely follows that predicted by the simple model. This effect demonstrates very clearly that the increase in the conductivity of the doped samples above 600 K is correlated with thermal detrapping from these traps.

A trapping energy (E_1) of about 1.1 eV is obtained for both samples and may be taken as characteristic of the high-temperature trap introduced by chromium doping. The large variations in the pre-exponential factor $(K_{-1}/K_1)_0$ are not significant since the factor compensates for the differences in E_1. The largest $(K_{-1}/K_1)_0$ values correspond to the largest E_1 values. This correspondence is also observed between the $(K_{-1}/K_1)_0$ and $(K_{-2}/K_2)_0$ values and the corresponding energy values E_1 and E_2 of the undoped samples. Because there is no systematic variation of $(K_{-1}/K_1)_0$ with the radiation flux ϕ for identical E_1 values, we see no evidence for radiation-induced detrapping.

2. *Undoped samples*

The RIC of the undoped samples were first fit over the temperature range from room temperature to past the maximum in σ neglecting the $(K_{-1}/K_1)_0$ term in Eq. (40). This procedure yielded I_1^0, I_2^0, $(K_{-2}/K_2)_0$, K_0^1, E_2, and E values. The I_1^0 value determined from the low-temperature fit was used as an initial value in fitting the high-temperature data over a range slightly over-lapping the low-temperature range. In the high-temperature fit $(K_{-2}/K_2)_0 \gg e$ so the I_2^0 term in Eq. (40) could be neglected. This procedure yielded I_1^0, $(K_{-1}/K_1)_0$, and E_1 values where the I_1^0 value agreed to within 10% with the low-temperature I_1^0 value. The low- and high-temperature I_1^0 values were then averaged

and the fitting procedure repreated over the two temperature regions with I_1^0 fixed at the average value. As indicated above, a fixed value of $K_{01} = 9.5\times10^{-11}$ cm^{3}sec^{-1} was used for the undoped samples.

The theoretical fit to the data, as shown in Figs. 7 and 8 for the undoped Meller and Linde samples, is generally quite good. It of course cannot reproduce all of the variations in the conductivity that result from the presence of additional traps not accounted for by the two-trap theory. The values of $\bar{\delta}(T)$ calculated from these fits (shown in Figs. 4 and 5) reproduce fairly well the general temperature dependence observed for the experimental values. This is not suprising, however, since the $\bar{\delta}_{10}(T)$ and $\bar{\delta}_{100}(T)$ values are the average rate of change of $\log_{10}\sigma$ as a function of $\log_{10}\phi$ for beam currents of 3 to 30 nA, and 30 to 300 nA, respectively. Therefore a good fit to $\bar{\delta}(T)$ follows automatically from properly fitting $\sigma(T)$. The predicted sequence in $\bar{\delta}$ of 1 to $\frac{1}{2}$ to 1 to $\frac{1}{2}$ with increasing temperature shown in Fig. 17 is approximately followed. The largest deviations from this behavior occur for $\bar{\delta}_{100}$ of the Meller sample between 600 and 900 K because of the large scatter in the experimental $\sigma(T)$ data at 300 nA over this temperature range. The low-temperature minimum in $\bar{\delta}$ occurs at a higher temperature for $\bar{\delta}_{100}$ than $\bar{\delta}_{10}$ as expected from the two-trap model (see Fig. 17).

It is instructive to compare the trapping parameter of the two undoped samples. These samples have approximately the same effective deep trap concentrations but the shallow trap concentration I_2^0 of the Meller sample is an order of magnitude larger than that of the Linde sample. Also, the low- and high-temperature traps controlling the RIC in the Meller sample are distinct from those of the Linde sample as indicated by the differences in the activation energies E_2 and E_1. The activation energies E ($E \simeq E_3 - E_2$) are also different in these samples, although the thermal activation energies E_3 for hole release of approximately 0.7 eV ($E_3 = E_2 + E$) are essentially the same.

E. Correlation of RIC activation energies with TSC activation energies

One can now attempt to correlate the activation energies E_1, E_2, and E_3 resulting from computer fits to the RIC data with the TSC activation energies shown in Table I. This correlation is indicated in Table V.

First we consider the E_2 and E_3 activation energies. Because the TSC measurements were performed above room temperature, the low-temperature TSC and thermoluminescence activation energies of Kawamura and Royce[23] and Cooke *et al.*[29] for a 270 K peak were averaged to give a value of 0.55 eV. The shallow trap activation energies E_2 of the Meller and Linde samples correlate with the TSC activation energies of 0.55 and 0.72 eV, respectively. The hole activation energy $E_3 = E_2 + E$ can be correlated with the TSC activation energy of 0.77 eV which corresponds to the 419-K TSC peak. This peak has been attributed to hole release from $V\bar{O}_H$ centers by Turner and Crawford[9] and by Lee *et al.*[19] in agreement with the isochronal annealing study of the Cr^{4+} EPR intensity discussed above. Therefore, if the thermal quenching mechanism is acting in these samples, it appears that hole release from intrinsic $V\bar{O}_H$ centers is responsible for the decreases observed in the conductivity with increasing temperature. The results of the Cr^{4+} isochronal annealing study have already been shown to be consistent with the assumption that the 0.70 eV shallow trap (396-K TSC peak) is an electron trap. The computer fits to the doped samples provide no information about E_2

TABLE V. Comparison of activation energies determined from theoretical fits to the radiation-induced-conductivity (RIC) and from thermally-stimulated-current (TSC) measurements.

Shallow trap			Intermediate trap			Deep trap			
RIC	TSC		RIC	TSC		RIC	TSC		
E_2 (eV)	E (eV)	T_{max} (K)	E_2+E (eV)	E (eV)	T_{max} (K)	E_1 (eV)	E (eV)	T_{max} (K)	Sample
0.70 ± 0.02	0.72 ± 0.1	396.0	0.75 ± 0.04	0.77 ± 0.1	419.0	1.5 ± 0.3	1.3 ± 0.1	728.0	Linde—undoped
0.57 ± 0.06	0.55 ± 0.1 [a]	273.0	0.67 ± 0.08	0.77 ± 0.1	419.0	4.3 ± 0.5	2.7 ± 0.2	1071.0	Meller—undoped
...	...	...	...	...	...	1.0 ± 0.1	1.2 ± 0.1	568.0	Linde—doped with 0.004-wt.% Cr_2O_3
...	...	...	...	...	...	1.1 ± 0.1	1.2 ± 0.1	568.0	Linde—doped with 0.028-wt.% Cr_2O_3

[a] Activation energy determined from averaging results of Kawamura and Royce (Ref. 23) and Cooke *et al.* (Ref. 29) for 273-K TSC and thermoluminescence peaks.

and E_3 because the shallow trap concentration I_2^0 was assumed to be negligible.

The correlation of the deep trap activation energies E_1 with TSC activation energies is more difficult. The E_1 value of ~1.1 eV for the doped samples correlates well with the TSC activation energy of 1.2 eV which is associated, most likely, with the thermal release of electrons from Cr^{2+} ions. The E_1 value of 1.5 eV for the undoped Linde sample can be correlated, within the errors of these RIC and TSC activation energies, with the major 1.3-eV TSC peak observed in this sample at 728 K. There is a difficulty with the very high E_1 value of 4.3 eV of the Meller sample which is much greater than the 2.7-eV activation energy of the 1103-K TSC peak. Above 1200 K the conductivity of the Meller sample decreased to an equilibrium value several minutes after the beam was turned on. This long time to reach equilibrium indicates that space charge effects may be introducing error into the high-temperature RIC values of the Meller sample.

F. Estimate of electron-capture cross section of hole traps

Before proceeding further, it is appropriate to estimate the cross section for trapping of electrons at the occupied hole traps (V_{OH}^- centers) assuming the thermal quenching model is correct. The cross section for electron capture is given by $\sigma_n = K_0/\langle v\rangle$, where K_0, the recombination rate at the occupied hole traps (concentration h_3), is less than rate $K_{01} = 9\times10^{-11}$ cm^{-3}/sec according to Eq. (38) and $\langle v\rangle$ is the mean thermal velocity of the electrons given by $\langle v\rangle = (3\ KT/m^*)^{1/2}$. The value of σ_n is then less than 7.2×10^{-18} cm^2 at 300 K where $\langle v\rangle$ is 1.2×10^7 cm/sec. This value represents a small cross section for electron capture such as might be expected to characterize electron capture by repulsive V_{OH}^- centers. Computer fits to the data only yield the ratios $(K_{-1}/K_1)_0$ and $(K_{-2}/K_2)_0$ so the electron capture rates K_1 and K_2 and their corresponding cross sections cannot be determined.

V. ADDITIONAL TEMPERATURE-DEPENDENT MECHANISMS

In the simple two-trap model it was assumed that the electron-hole generation rate ϕ, the electron-hole recombination rate K_0 at the hole traps, the electron capture rates K_1 and K_2 at the electron traps, and the electron mobility were constants independent of temperature. It is now appropriate to examine the possibility that these parameters are also temperature dependent in order to determine the extent to which their temperature dependence might affect the conductivity. It will be shown below that there is no clear evidence that geminate recombination is causing a temperature-dependent generation rate ϕ. However, there is a possibility that either electron-hole recombination through multiphonon emission (MPE) or LO-phonon scattering of electrons could be responsible for the weak decreases in the conductivity observed with increasing temperature. Therefore, these last two mechanisms could serve as alternatives to that of thermal quenching by hole release.

Since MPE capture and LO-phonon scattering are characterized by activation energies on the order of 0.1 eV they must still be combined with the simple two-trap model without thermal quenching [Eq. (12)] to account for the large E_1 and E_2 activation energies. [If there is no thermal quenching $K_4 = 0$, $K_{01} = K_0$, and $K_0^1 = 0$ from Eqs. (38) and (39), and Eq. (40) reduces to Eq. (12).]

A. Temperature-dependent electron-hole generation rate: Geminate recombination

The possibility of a temperature-dependent generation rate ϕ should be examined since the temperature-dependent changes in ϕ would also be reflected in the conductivity data. In a number of low mobility solids such as anthracene,[30-32] yields of electron-hole pairs from ionizing radiation have been explained by the theory of geminate or initial recombination developed for gases by Langevin[33] and Onsager.[34] Classically, the electron (hole) becomes trapped in the Coulomb field of the hole (electron) if the electron is closer than the critical Onsager escape radius $r_c = e^2/4\pi\epsilon\epsilon_0 kT$. For Al_2O_3, r_c is 57 Å at 300 K using $\epsilon = 10$. If the initial separation r_0 (the thermalization length) of the electron and hole is less than r_c after they come into thermal equilibrium with the lattice, the pair will diffuse together and recombine. The application of a large electric field can drive the particles in opposite directions, enhancing the yield. At low fields the free carrier yield is given by

$$G_\infty(E) = \phi_0[\exp(-r_c/r_0)][1+(e^3/8\pi\epsilon\epsilon_0 k^2T^2)E], \tag{41}$$

where ϕ_0 is the limiting carrier yield at high fields E.[35] For Al_2O_3 the slope to intercept ratio $(e^3/8\pi\epsilon\epsilon_0 k^2T^2)$ at 300 K is 1.1×10^{-5} cm/V. Therefore electric-field-dependent carrier yields are not expected to be significant until E is greater than about 10^4 V/cm. As the temperature increases at low fields the exponential term in Eq. (41) dominates and the carrier yield increases, as has been observed in anthracene by Saleh[32] and in selenium by Pai and Enck.[36] There was no field dependence observed in our 300-K RIC values be-

tween 1 and 3×10^3 V/cm, as expected. However, the observed decreases in the conductivity with increasing temperature are contrary to Eq. (41) which would predict an increasing RIC. It has been noted that the thermalization length r_0 increases with increasing excitation energy.[28,36] Because we are utilizing 1.5-MeV electrons to generate electron-hole pairs it is possible that r_0 is greater than r_c so that the electron-hole pairs do not recombine. Another possibility is that the mean free path of the electron is sufficiently long for the electron not to diffuse towards the hole.

Since there is no clear evidence of geminate recombination of the electron-hole pairs it is not surprising that the magnitude of the bulk recombination rate K_0 gives no indication of diffusion-controlled recombination: the K_0 value determined from computer fits to the data is less than 9.5×10^{-11} cm^3sec^{-1} while the Langevin rate constant $\gamma=4\pi e\mu/4\pi\epsilon\epsilon_0$ is 1.8×10^{-7} cm^3sec^{-1}. Both of these rate constants were determined assuming an electron mobility of 1 cm^2/V sec. The Langevin rate expression is only valid for a mean free path $\lambda \ll r_c$. If the mobility at 300 K lies between 5 and 50 cm^2/V sec, for example, one finds mean free times of 3×10^{-15} to 3×10^{-14} sec using the expression $\mu=e\tau/m^*$ and assuming that the effective mass m^* is the free electron mass. The mean free paths, $\lambda=\langle v\rangle\tau$, then range between 3 and 30 Å as compared to $r_c=57$ Å for Al_2O_3. The discrepancy between the Langevin rate and the experimental recombination rate K_{01} may result from λ being too large compared to r_c. If this is the case, as it is for high mobility semiconductors, the electrons cannot be assumed to be diffusing toward trapped holes. If the mobility is sufficiently low so that $\lambda \ll r_c$, then the discrepancy between the Langevin rate and the bulk recombination rate K_0 provides further evidence that recombination is occurring with holes trapped at sites such as V_{OH} centers which act as repulsive electron traps. The Langevin rate would not describe this situation since its derivation is based on the assumption that electrons recombine with holes under the influence of Coulomb attraction.

B. Temperature-dependent capture cross sections: Multiphonon emission

Nonradiative recombination occurring at impurities in semiconductors can take place by multiphonon emission (MPE). In the case of GaAs and GaP Henry and Lang have recently found that the majority of the capture cross sections determined by the deep-level transient spectroscopy (DLTS) technique can be attributed to MPE.[37] At high temperatures their theory gives for the cross section $\sigma=\sigma_\infty \exp(-E_\infty/kT)$, where $\sigma_\infty=10^{-14}$ to 10^{-15} cm^2 for neutral centers. This result is in basic agreement with earlier estimates of $\sim6\times10^{-15}$ cm^2 for σ_∞ of neutral and attractive centers by Sinyavskii *et al.*[38] Ridley[39] and Passler[40-41] have pointed out that below approximately 1000 K, intermediate- and low-temperature expressions for the capture cross section are more relevant than the above σ_∞ expression because the conditions pertaining to the high-temperature limit may be difficult to achieve in practice. Therefore a single temperature-independent activation energy E_∞ cannot be expected to describe the MPE capture cross section σ over the temperature range of our measurements (300–1300 K). Indeed, the MPE activation energy $E_{MPE}(T)$ can decrease to a fraction of its high-temperature value E_∞ as the capture cross section approaches a plateau region at low temperature.[37,40] As we have pointed out above in our two-trap theory, the free-electron concentration e depends only on the ratio of the thermal detrapping rates to the trapping rates K_{-2}/K_2 and K_{-1}/K_1 [Eq. (40)]. If electron capture occurs through an MPE process then, considering just the deepest trap, $K_1\sim\exp(-E_{MPE}/kT)$ so that $K_{-1}/K_1 \sim(E_{MPE}-E_1)/kT$. Since E_{MPE} is typically only a fraction of the true level depth E_1,[42] the temperature dependence of E_{MPE} would not have a significant effect on the ratio K_{-1}/K_1. The model would therefore be correct in assigning the major temperature dependence to the thermally activated detrapping coefficients K_{-1} and K_{-2}.

However, if electron capture at the occupied hole traps (h_3) occurs through MPE, then $K_0 \sim \exp[-E_{MPE}(T)/kT]$ resulting in an observable decrease in the RIC as the temperature increases [see Eq. (12)]. The room-temperature value of the electron capture cross section has been shown above to be less than 7×10^{-18} cm^2 in the 0.004-wt.%-Cr_2O_3-doped sample. Since this value is of the same order of magnitude as a number of room-temperature cross sections attributed to MPE capture by Henry and Lang,[37] it is possible that bulk recombination is occurring at the hole traps through an MPE process. If this is the case, then the weak decreases observed with increasing temperature could result from the temperature dependence of the recombination rate K_0. Also, the fact that E_{MPE} increases at high temperatures could provide an explanation for the curvature observed in plots of $\log_{10}\sigma$ versus inverse temperature (see Figs. 9 and 10) for the chromium-doped samples between 300 and 600 K.

C. Temperature-dependent mobility: LO-phonon scattering

In a polar crystal such as Al_2O_3 it is generally assumed that the mobility is controlled by LO-

phonon scattering. Lynch[43] has shown that calculations by Howarth and Sondheimer[44] and a number of other authors[45-47] reduce to a common mobility expression

$$\mu_1 = (\hbar/2m_e)(1/\alpha)(e/\hbar\omega_1)\exp(\hbar\omega_1/kT) \qquad (42)$$

for $\hbar\omega_1 > kT$. In this expression $\hbar\omega_1$ is the energy of the phonon mode, α is the electron-lattice coupling constant and m_e is the electron effective mass. For a given phonon mode, α is given by

$$\alpha = (1/\epsilon_H - 1/\epsilon_L)(e^2/\hbar)(m/2\hbar\omega_1)^{1/2}, \qquad (43)$$

where ϵ_H and ϵ_L are the dielectric constants on the high- and low-frequency side of the mode frequency. Utilizing the infrared data of Barker[48] for Al_2O_3, the α values of each mode were calculated from Eq. (43). The ϵ_H, ϵ_L values used in the calculations were determined by progressively incrementing the high frequency dielectric constant ϵ_∞ by Barker's values for the oscillator strength $\Delta\epsilon_i$ of each mode where the low-frequency dielectric constant $\epsilon_0 = \epsilon_\infty + \sum_i \Delta\epsilon_i$. For example, ϵ_∞ for the A_{2u} modes is 3.1 and $\Delta\epsilon$ for the highest-frequency A_{2u} LO-phonon mode (26.1 THz) is 1.7 giving $\epsilon_H = 3.1$ and $\epsilon_L = 4.8$ for this mode. The α and μ_1 values at 300 K for each mode are shown in Table VI where the effective electron mass has been assumed to be equal to the free electron mass. A total mobility of 26 cm^2/V sec then results from applying Matthiessen's rule to the individual modes. It is interesting to note that the 0.064- and 0.077-eV modes control the room temperature mobility because they are more populated than the strongly-coupled 0.108-eV mode. This room-temperature mobility is much larger than the value of 3 ± 1 cm^2/V sec recently reported by Hughes[16] for an undoped c-axis Linde sample. Feynman *et al.*[49] and Thornber and Feynmann[50] have also derived a mobility expression which is given by $\mu_2 = 1.5(kT/\hbar\omega_1)\mu_1$. When this expression is used for each mode a room-temperature mobility of 13 cm^2/V sec results which is still a factor of 4 higher than the Hughes result. In SiO_2, which has a phonon spectrum similar to that of Al_2O_3, the drift mobility measured by Hughes was approximately 22 cm^2/V sec at room temperature in comparison to a LO-phonon mobility of 32 cm^2/V sec calculated by Lynch[40] using the Feynman mobility expression μ_2. The agreement of the theoretical result with Hughes mobility value is therefore much worse in the case of Al_2O_3. Part of this discrepancy could be caused by an effective mass considerably larger than the free electron mass. It is also possible that the Hughes mobility measurement may be trap controlled such as can occur when a sample contains a high concentration of shallow traps. Our fits of the two-trap model to the RIC data indicate that both the undoped Linde and Meller samples have a high shallow trap concentration. A Hall measurement in this case would give the true "microscopic" mobility. A Hall measurement by Green[51] gave a much higher value of ~90 cm^2/V sec. However, the details of the measurement were not specified so it is difficult to judge the accuracy of this value.

Because the above factors may introduce uncertainty in the magnitude of the mobility it is generally only possible to consider the temperature dependence of the mobility which is, in any case, the primary concern in our studies. If one assumes that the decrease in the conductivity of the 0.004-wt.%-Cr_2O_3-doped sample solely reflects the temperature dependence of the LO-phonon scattering, the temperature dependence of the conductivity data of this sample and the mobilities μ_1 and μ_2 can be compared as shown in Fig. 20. In this plot the conductivity and mobility values are normalized to their room temperature values. The temperature dependence of the conductivity is almost identical to the μ_1 dependence. The Feynman mobility μ_2 predicts a much less rapid de-

TABLE VI. Calculated coupling constants and mobilities for LO-phonon modes.

LO-phonon frequencies ν_i [a] (THz)	Phonon energy $h\omega_i$ (eV)	Coupling constant α	Mobility μ_1 (300 K) ($cm^2V^{-1}sec^{-1}$)	Mobility μ_2 (300 K) ($cm^2V^{-1}sec^{-1}$)
11.6	0.048	0.03	2.4×10^3	1.9×10^3
14.4	0.060	0.66	1.5×10^2	9.7×10^1
15.4	0.064	1.76	6.1×10^1	3.4×10^1
18.7	0.077	1.66	9.1×10^1	4.5×10^1
26.1	0.108	1.25	2.8×10^2	1.0×10^2
27.0	0.112	0.38	1.0×10^3	3.6×10^1

[a] LO-phonon frequencies from Barker (Ref. 48).

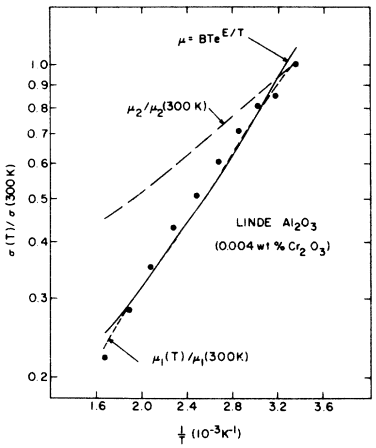

FIG. 20. Temperature dependence of the normalized RIC values of the 0.004-wt.%-Cr_2O_3-doped sample. Also shown are the normalized Howarth-Sondheimer mobility $\mu_1(T)/\mu_1(300\ K)$, the normalized Thornber-Feynman mobility $\mu_2(T)/\mu_2(300\ K)$, and the empirical mobility expression $\mu = BT\exp(E/kT)$, where $B = 5.0\times10^{-5}$ cm^2/V sec K and $E = 0.11$ eV.

crease in the conductivity with increasing temperature than is observed. However, if a single temperature-independent activation energy of $E = \hbar\omega_1 = 0.11$ eV is used in the Feynman expression, the temperature dependence of the conductivity and the Howarth-Sondheimer mobility μ_1 can be approximately simulated as shown in Fig. 20. Therefore, the expression $\mu = BT\exp(E/kT)$ with an effective activation energy E and a constant coefficient B serves as an empirical mobility expression which can be useful in performing computer fits to the data. The conductivities of the doped and undoped samples were fit between 300 K and the temperature of their conductivity minima. It was assumed that decreases in the conductivity solely resulted from the temperature dependence of the mobility without thermal quenching.

In the doped samples, Eq. (12) shows that e is constant over this temperature region because the I_2^0 term can be neglected and $K_{-1}/K_1 \ll e$. Therefore all of the temperature dependence results from the mobility μ. The normalized RIC values $\sigma(T)/\sigma(300\ K)$ for these samples could then be fit with the empirical mobility expression since the e values cancelled out. Because the normalized RIC values are practically independent of beam current, the individual values at 3, 30, and 300 nA were first averaged and then fit to $\mu = BT\exp(E/kT)$. In this way B is normalized to give a mobility of approximately 1 cm^2/V sec at 300 K. The $\sigma(T)$ values resulting from these fits are reasonably good approximations to the RIC data as shown in Figs. 9 and 10 for the doped samples. The recombination rates K_0 were calculated from Eq. (12). The K_0 and B values for the lightly doped sample (shown in Table VII) were used as starting parameters for fitting the RIC data of the undoped samples.

The solutions of Eq. (12) for the free-electron concentration e were multiplied by the mobility $\mu = BT\exp(E/kT)$ in fitting the RIC of the undoped samples. In these fits the K_{-1}/K_1 term in Eq. (12) was neglected. The resulting parameters shown in Table VII represent averages of the parameters obtained for beam currents of 3, 30, and 300 nA. The fits to the RIC data, shown in Figs. 7 and 8, are good considering the approximation used for the mobility.

It is instructive to examine the parameters of the doped and undoped samples. Once again the fits indicate that $I_2^0 \gg I_1^0$ for the undoped samples. The results for the activation energies E_2 and E are of the greatest interest. The values of E_2 for the undoped samples are the same as the values derived using the thermal quenching model (see Table IV) within the accuracy of the fits. Therefore, the correspondence shown in Table V between the E_2 values and the activation energies of specific TSC peaks still applies. Also, the undoped and lightly doped samples have the same value of $E \simeq 0.11$ eV independent of their respective E_2, I_1, and I_2 values. As was pointed out above, with $E = 0.11$ eV the empirical mobility $\mu = BT\exp(E/kT)$ has a temperature dependence approximating that calculated above for the Howarth-Sondheimer LO-phonon scattering mobility μ_1. Therefore it is possible that a mobility controlled by LO-phonon scattering is responsible for the decreases in the conductivity observed with increasing temperature rather than thermal quenching or a temperature-dependent MPE electron-hole recombination rate.

Although LO-phonon scattering may be limiting the electron mobility at elevated temperatures, the room temperature RIC data of the undoped and chromium-doped samples provide no clear evidence that this is true at lower temperatures ($T < 300$ K). In the case of LO-phonon scattering, the RIC of the chromium-doped samples should continue to increase rapidly at low temperatures. However the RIC of the chromium-doped samples shows signs of leveling off at room temperature (see Figs. 9 and 10). At sufficiently low temperature the RIC of the undoped samples should also increase. At the highest dose rate (6.6×10^4 rad/sec) the RIC of these samples has leveled off near room temperature (see Figs. 7 and 8). A constant RIC at low temperatures would be consistent with the temperature-independent mobility value of 3 $\pm 1\ cm^2/V$ sec reported by Hughes[16] for an undoped

TABLE VII. Parameters of the two-trap model with LO-phonon scattering.

	I_1^0 (cm^{-3})	I_2^0 (cm^{-3})	K_{01} ($cm^{-3}sec^{-1}$)	B[a] ($cm^2V^{-1}sec^{-1}K^{-1}$)	$\log_{10}(K_{-2}/K_2)_0$[b]	E_2 (eV)	E (eV)
Linde (undoped)	$(1.6 \pm 0.4) \times 10^{16}$	$(2.5 \pm 1.2) \times 10^{17}$	$(9.6 \pm 1.5) \times 10^{-11}$	$(4.4 \pm 0.3) \times 10^{-5}$	21.0 ± 0.3	0.71 ± 0.03	0.11 ± 0.01
Meller (undoped)	$(8.6 \pm 2.6) \times 10^{15}$	$(1.7 \pm 0.2) \times 10^{18}$	$(9.1 \pm 0.3) \times 10^{-11}$	$(4.9 \pm 0.3) \times 10^{-5}$	19.3 ± 0.2	0.61 ± 0.03	0.12 ± 0.01
Linde (0.004-wt.% Cr_2O_3)	2.6×10^{17}	...	1.3×10^{-10}	5.0×10^{-5}	...	...	0.11
Linde (0.03-wt.% Cr_2O_3)	1.8×10^{18}	...	1.2×10^{-10}	9.5×10^{-5}	...	...	0.09

[a] Coefficient B gives an electron mobility $\mu_e = BT^2e^{E/kT}$ at 300 K of 1.0 ± 0.5 $cm^2V^{-1}sec^{-1}$ for the Linde samples and 1.5 ± 0.7 $cm^2V^{-1}sec^{-1}$ for the Meller sample.
[b] $(K_{-2}/K_2)_0$ is in cm^{-3}.

Linde sample between 100 and 350 K. At present it is not clear what mechanism could be responsible for a constant low-temperature mobility.

VI. SUMMARY

Measurements of the steady-state conductivity of single crystal Al_2O_3 samples during electron irradiation show a complicated temperature dependence. As the temperature increases there are regions in which the RIC is rapidly increasing with activation energies between 0.6 and 4.3 eV and regions in which it is slowly decreasing with an activation energy of approximately 0.1 eV. A simple two-trap model was developed which associates the increases in the RIC with the thermal release of electrons from shallow traps (activation energy E_2) at low temperatures and from deep traps (activation energy E_1) at the highest temperatures. The model was extended to include the possibility of thermal quenching of the conductivity through hole release at intermediate temperatures. Computer fits to the data using the simple two-trap model with thermal quenching gave values for the major activation energies E_2 and E_1 which, for the most part, could be correlated with specific trap activation energies determined from TSC measurements. The values for E_2 and E_1 appear to be insensitive to the exact mechanism proposed for the weak decreases in the conductivity. This point was demonstrated when almost identical E_2 values for the undoped samples were obtained from fits to the RIC data including either a thermal quenching term or an LO-phonon scattering mobility term to describe the decreasing conductivity. The following conclusions regarding the shallow and deep electron traps were reached:

(i) The conductivity of the undoped Linde and Meller samples is controlled by their high concentration of shallow traps with activation energies of 0.57 and 0.72 eV, respectively.

(ii) The conductivity of the chromium-doped samples is controlled by the high concentration of deep 1.2-eV electron traps which suppress the low-temperature increase in the conductivity observed in the undoped samples. In our model these traps are Cr^{3+} ions which are converted to Cr^{2+} ions after trapping electrons.

An isochronal annealing study of Al_2O_3 samples γ irradiated at room temperature supported the sequence of charge release assumed in the model, i.e., electron release at low temperatures followed by hole release at higher temperatures. The first major TSC peak occurring above room temperature, the 396-K (0.72-eV) peak, is associated with electron release and the 419- and 509-K TSC peaks are identified with hole release, in agreement with the Turner and Crawford[9] and Lee

et al.[10,19] assignment of these peaks to hole release from V_{OH}^- and V^{2-} hole traps.

The slow decreases in the conductivity observed with increasing temperature can result from a number of mechanisms including thermal quenching by holes released at intermediate temperatures, electron-hole recombination through multiphonon emission, or LO-phonon scattering of conducting electrons. If one assumes that only one mechanism is responsible for the decrease in the conductivity, the following conclusions are possible:

(a) If the thermal quenching mechanism is dominant, then hole release from V_{OH}^- centers is probably responsible for the decreases in the conductivity of the undoped samples.

(b) The value of the bulk electron-hole recombination rate K_0 was determined from computer fits to the RIC data to be less than 9×10^{-11} cm^3/sec (electron capture cross section less than 7×10^{-18} cm^2) for the 0.004-wt.%-Cr_2O_3-doped sample assuming an electron mobility of 1 cm^2/V sec. This recombination rate would not be unusual for electron-hole recombination occurring through an MPE process at repulsive hole centers such as V_{OH}^- centers.

(c) Computer fits to the RIC data indicate that if the LO-phonon scattering mechanism is dominant at elevated temperatures then the Howarth-Sondheimer "large polaron" mobility (μ_1) most accurately represents the temperature dependence of the mobility.

ACKNOWLEDGMENTS

We are grateful to Marilyn McKeown for her assistance with the computer programming. We also would like to thank R. C. Hughes for technical discussions and for sending a preprint of his work. The technical assistance of Albert Pinelli and James Hurst, Jr. is also appreciated. This work has been supported by the U.S. Department of Energy under Contract EY-76-C-02-0016.

*Now at Kirtland Air Force Base, Albuquerque, New Mexico 87117.

[1]D. G. Martin, J. Phys. Chem. Solids 10, 64 (1958).

[2]J. J. Antal and A. N. Goland, Phys. Rev. 112, 103 (1958).

[3]E. W. Mitchell, J. D. Rigden, and P. W. Townsend, Philos. Mag. 5, 1013 (1960).

[4]G. W. Arnold and W. D. Compton, Phys. Rev. Lett. 4, 66 (1960).

[5]P. W. Levy, Phys. Rev. 123, 1226 (1961).

[6]F. T. Gamble, R. H. Bartram, C. G. Young, and O. R. Gilliam, Phys. Rev. 138, A577 (1965).

[7]J. M. Bunch and F. W. Clinard, Jr., J. Am. Ceram. Soc. 57, 279 (1974).

[8]G. W. Arnold, G. B. Krefft, and C. B. Norris, Appl. Phys. Lett. 25, 540 (1974).

[9]T. J. Turner and J. H. Crawford, Jr., Solid State Commun. 17, 167 (1975).

[10]K. H. Lee, G. E. Holmberg, and J. H. Crawford, J. Solid State Commun. 20, 183 (1976).

[11]K. H. Lee and J. H. Crawford, Jr., Phys. Rev. B 15, 4065 (1977).

[12]B. D. Evans and M. Stapelbrock, Phys. Rev. B 18, 7089 (1978).

[13]Special Purpose Materials for the Fusion Reactor Environment, Report No. DOE/ET-0015 (1978) (unpublished).

[14]D. J. Huntley and J. R. Andrews, Can. J. Phys. 46, 147 (1968).

[15]V. A. J. van Lint, J. W. Harrity, and T. M. Flanagan, IEEE Trans. Nucl. Sci. NS-15, 194 (1968).

[16]R. C. Hughes, Phys. Rev. B 19, 5318 (1979).

[17]J. G. Simmons, G. S. Nadkarni, and M. C. Lancaster, J. Appl. Phys. 41, 2 (1970).

[18]M. J. Berger and S. M. Seltzer, Tables of Energy Losses and Ranges of Electrons and Positrons, Report No. NASA SP-3012 (1964) (unpublished).

[19]K. H. Lee, G. E. Holmberg, and J. H. Crawford, Jr., Phys. Status Solidi A 39, 669 (1977).

[20]W. Hoogenstraaten, Philips Res. Rep. 13, 515 (1958).

[21]G. F. J. Garlick and A. F. Gibson, Proc. Phys. Soc. London 60, 574 (1948).

[22]P. Kivits and H. J. L. Hagebeuk, J. Lumin. 15, 1 (1977).

[23]S. Kawamura and B. S. H. Royce, Final Technical Report on NSF Contract No. DMR-75-02988, Princeton University, 1978 (unpublished).

[24]R. H. Hoskins and B. H. Soffer, Phys. Rev. 133, A490 (1964).

[25]M. A. Brown, J. Phys. C 9, 1955 (1976).

[26]M. Abou-Ghantous, I. A. Clark, and W. S. Moore, J. Phys. C 9, 1965 (1976).

[27]P. R. Bevington, *Data Reduction and Error Analysis for the Physical Sciences* (McGraw-Hill, New York, 1969).

[28]R. C. Hughes, Solid State Electron. 21, 251 (1978).

[29]D. W. Cooke, H. E. Roberts, and C. Alexander, Jr., J. Appl. Phys. 49, 3451 (1978).

[30]R. G. Kepler and F. N. Coppage, Phys. Rev. 151, 610 (1966).

[31]R. C. Hughes, J. Chem. Phys. 55, 5442 (1971).

[32]M. Saleh, J. Phys. C 9, 4165 (1976).

[33]P. Langevin, Ann. Chem. Phys. 28, 287 (1903); 28, 433 (1903).

[34]L. Onsager, Phys. Rev. 54, 554 (1938).

[35]C. R. Gruhn and M. D. Edmiston, Phys. Rev. Lett. 40, 407 (1978).

[36]D. M. Pai and R. C. Enck, Phys. Rev. B 11, 5163 (1975).

[37]C. H. Henry and D. V. Lang, Phys. Rev. B 15, 989 (1977).

[38]E. P. Sinyavskii and V. A. Kovarskii, Fiz. Tverd. Tela 9, 1464 (1966) [Sov. Phys. Solid State 9, 1142 (1967)].

[39]B. K. Ridley, J. Phys. C 11, 2323 (1978).

[40]R. Pässler, Phys. Status Solidi B 85, 203 (1978).
[41]R. Pässler, Phys. Status Solidi B 86, K39 (1978).
[42]D. V. Lang and R. A. Logan, J. Electron. Mater. 4, 1053 (1975).
[43]W. T. Lynch, Ph.D. thesis, Princeton, 1971 (unpublished).
[44]D. J. Howarth and E. H. Sondheimer, Proc. R. Soc. London 219, 53 (1953).
[45]H. Fröhlich, Adv. Phys. 3, 325 (1954).
[46]R. Stratton, Proc. R. Soc. London Ser. A 246, 406 (1958).
[47]L. P. Kadanoff, Phys. Rev. 130, 1364 (1963).
[48]A. S. Barker, Jr., Phys. Rev. 132, 1475 (1963).
[49]R. P. Feynman, R. W. Hellwarth, C. K. Iddings, and P. M. Platzman, Phys. Rev. 127, 1004 (1962).
[50]K. K. Thornber and R. P. Feynman, Phys. Rev. B 1, 4099 (1970).
[51]B. A. Green and M. V. Davis, Trans. Am. Nucl. Soc. 16, 75 (1973).